Climate Dynamics (2025) 63:231
https://doi.org/10.1007/s00382-025-07704-w

How well CMIP6 models simulate key boundary conditions affecting South American climate? Insights for regional modeling efforts

Paola A. Arias[1] · Isabel C. Correa[1] · Lluís Fita[2,3,4] · J. Alejandro Martínez[5] · Camila Alvarez-Garreton[6] · Lincoln M. Alves[7] · Juan P. Boisier[6,8] · Lenin Campozano[9,10] · Jhan-Carlo Espinoza[11,12] · Clementine Junquas[11] · Marta Llopart[13] · Anna A. Sörensson[2,3,4]

Received: 15 November 2024 / Accepted: 16 April 2025 / Published online: 16 May 2025

Abstract

South America is a large continent with a wide diversity of weather and climate features, including tropical, subtropical and extratropical regimes interacting within a complex landscape. Simulations by global climate models, as well as their downscaling through regional circulation models or statistical methods, are important tools, particularly when assessing the impacts of climate change in the continent. This work evaluates 57 models of the sixth phase of the Coupled Model Intercomparison Project (CMIP6) in their simulation of various spatial patterns and circulation features over South America. Our evaluation aims to provide useful input for the selection of climate models to force regional simulations in South America. Therefore, we focus on spatial fields that are relevant for regional simulations, such as horizontal winds, sea level pressure, sea surface temperature (SST), and moisture and energy fluxes across the domain boundaries. Additionally, we evaluated different circulation features influencing the regional climate of South America that have not been widely evaluated in these models. Several indices are studied to assess the main low-level and upper-level continental-scale circulation patterns, the regional Walker and Hadley cells, the subtropical highs and the boundary SST patterns. Our results show that no single model performs best across all evaluated features, highlighting the importance of in-depth model evaluation for the region concerning the features of interest.

Keywords South America · CMIP6 · Model evaluation · Regional circulation · Regional simulations

✉ Paola A. Arias
paola.arias@udea.edu.co

[1] Grupo de Ingeniería y Gestión Ambiental (GIGA), Escuela Ambiental, Facultad de Ingeniería, Universidad de Antioquia, Medellín, Colombia

[2] Facultad de Ciencias Exactas y Naturales, Universidad de Buenos Aires, Buenos Aires, Argentina

[3] Centro de Investigaciones del Mar y la Atmósfera (CIMA), CONICET–Universidad de Buenos Aires, Buenos Aires, Argentina

[4] Instituto Franco-Argentino Para el Estudio del Clima y sus Impactos (UMI 3351 IFAECI), CNRS–IRD–CONICET–UBA, Buenos Aires, Argentina

[5] Escuela Ambiental, Facultad de Ingeniería, Universidad de Antioquia, Medellín, Colombia

[6] Center for Climate and Resilience Research CR2, FONDAP/ANID 1523A0002, Santiago, Chile

[7] National Institute for Space Research (INPE), São Paulo, Brazil

[8] Department of Geophysics, University of Chile, Santiago, Chile

[9] Departamento de Ingeniería Civil y Ambiental, Facultad de Ingeniería Civil y Ambiental, Escuela Politécnica Nacional, Quito 170517, Ecuador

[10] Grupo de Investigación, MetClima, Escuela Politécnica Nacional, Quito 170517, Ecuador

[11] University of Grenoble Alpes, IRD, CNRS, Grenoble INP, Institut des Géosciences de l'Environnement (IGE, UMR 5001), Grenoble, France

[12] Instituto de Investigación Sobre la Enseñanza de las Matemáticas, Pontificia Universidad Católica del Perú, 15088 Lima, Peru

[13] Universidade Estadual Paulista (UNESP), Bauru, SP, Brazil

1 Introduction

South America is a large continental mass hosting 13 countries and extending over about 18 million km^2. This continent spans latitudes from approximately 15° N to 60° S, resulting in a diverse range of weather and climate features, including tropical, subtropical and extratropical regimes. On the western side, the Andes mountain range is the most prominent orographic feature, extending continuously from the south to the north of the continent. It is the longest cordillera and one of the most biodiverse regions in the world (e.g. Hoorn et al. 2010; Rangel et al. 2018). The interactions between the steep topography and the incoming winds from the adjacent oceans and the inner continent allow different diurnal and seasonal hydrological regimes at both sides of the Andes (e.g. Poveda et al. 2005; Garreaud 2009; Espinoza et al. 2015, 2020; Rau et al. 2016; Junquas et al. 2018; Viale et al. 2019; Arias et al. 2021a). In particular, the easterly flow coming within the Trade Winds has an important influence over northern South America (e.g. Poveda et al. 2006; Segura et al. 2019) while the Westerlies and large-scale perturbations developing in the extratropics dominate the weather and climate variability of the southern part of the continent (e.g. Viale and Garreaud 2015). In the upper troposphere (about 200–300 hPa), the most prominent features are an anticyclonic circulation during austral summer (December–February, DJF), known as the Bolivian High (BH), two compensating cyclonic centers to the west (producing convergence over the Peruvian and Ecuadorian coasts) and the east (a.k.a the Nordeste Low) of the BH, and the Southern Hemisphere Subtropical and Polar Jets (e.g. Lenters and Cook 1997; Sulca et al. 2016; Segura et al. 2020).

In interaction with the Andes, the development of low-level jets (LLJs) is among the main regional atmospheric circulation features in South America (e.g. Espinoza et al. 2020). The northern continent is influenced by the Caribbean LLJ in the north (e.g. Wang 2007; Amador 2008), the Choco LLJ by the west (e.g. Poveda and Mesa 1999; Yepes et al. 2019), and the Orinoco LLJ by the east (e.g. Torrealba and Amador 2010; Jiménez-Sánchez et al. 2019; Martínez et al. 2022). Towards the south, several regions at the east of the Andes are affected by the South American LLJ (e.g. Marengo et al. 2004; Vera et al. 2006a), while a LLJ that forms over the southeastern Pacific affects the regions along the western slope of the Andes (Garreaud and Muñoz 2005; Muñoz and Garreaud 2005). These LLJs control the atmospheric moisture transport and distribution within the continent and are key drivers of tropical-extratropical interactions (e.g. Salio et al. 2007; Sakamoto et al. 2011; Martinez and Dominguez 2014; Poveda et al. 2014; Arias et al. 2015; Espinoza et al. 2015; Gimeno et al. 2016; Chavez and Takahashi 2017; Hoyos et al. 2018; Morales et al. 2021). The intensity of the South American LLJ modulates the spatio-temporal variability of precipitation in Southeastern South America (SESA; mainly Argentina, and Uruguay) and southern Brazil, where a clear dipole pattern is described at several temporal scales between SESA and the continental South Atlantic Convergence Zone (SACZ) (Doyle and Barros 2002; Junquas et al. 2012). On the western side of the Andes, the Humboldt current and the associated upwelling of cold, nutrient-rich waters interact with low-level flows of the South Pacific Anticyclone, which modulates winds and rainfall regimes at several time-scales (e.g. Takahashi 2012; Garreaud 2018).

Ocean–atmosphere interactions and global climate variability modes affect South American climate at different time scales. The El Niño-Southern Oscillation (ENSO) is the main driver of interannual climate variability, with very diverse impacts across the continent (e.g. Aceituno 1988; Cai et al. 2020; Poveda et al. 2020). The Atlantic sea surface temperatures (SSTs) also contribute to interannual climate variability in South America, mainly over the northern, tropical and southeastern regions (e.g. Vuille et al. 2000; Taschetto and Wainer 2008; Yoon and Zeng 2010; Campozano et al. 2018; Arias et al. 2020, 2021a; Espinoza et al. 2022). The Southern Annular Mode is another important driver of sub-annual to interannual climate variability in the southern part of the continent (Gillett et al. 2006; Garreaud et al. 2009; Silvestri and Vera 2009; Boisier et al. 2016; Aceituno et al. 2021). Decadal modes of variability also determine climate variability in the continent, particularly the Pacific Decadal Oscillation and the Atlantic Multidecadal Oscillation (Jacques-Coper and Garreaud 2015; Kayano and Capistrano 2014; Boisier et al. 2016; Segura et al. 2016, 2020; Jones and Carvalho 2018; Stuecker 2018; Kayano et al. 2019, 2022; Campozano et al. 2020; Garreaud et al. 2020; Imfeld et al. 2020; Loaiza-Cerón et al. 2020). These different large-scale modes of variability influence South American climate through regional perturbations of the Hadley and Walker cells (e.g. Tedeschi and Collins 2015; Barichivich et al. 2018; Espinoza et al. 2019; Cai et al. 2020; Rao et al. 2022), and teleconnections across the southern Pacific. Moreover, surrounding oceans not only influence climate variability in South America but also constitute a primordial source of atmospheric moisture toward the continent (Drumond et al. 2008, 2010; Sakamoto et al. 2011; Gimeno et al. 2012; Martinez and Dominguez 2014; Poveda et al. 2014; Arias et al. 2015; Hoyos et al. 2018; Escobar et al. 2022; Leyba et al. 2023).

Different studies have evaluated the performance of global climate models in representing weather and climate in South America. Most of these studies focus on the

seasonal cycles of temperature and precipitation, as well as their variability and trends (see some recent studies: Rivera and Arnould 2020; Vasconcellos et al. 2020; Almazroui et al. 2021; Arias et al. 2021b; Díaz et al. 2021; Ortega et al. 2021; Vale et al. 2021; Varuolo-Clarke et al. 2021; Vicente-Serrano et al. 2022; Marianetti et al. 2024). In particular, the South American monsoon system (SAMS), one of the most distinctive climate features in the continent (e.g. Zhou and Lau 1998; Vera et al. 2006b), has been extensively assessed using models (Jones and Carvalho 2013; Seth et al. 2013; Prado et al. 2013; Rojas et al. 2016; Díaz and Vera 2018; Londoño-Arteaga and Lima 2021; Monteverde et al. 2022). Other studies have addressed temperature and precipitation extremes in models (Müller et al. 2018; Dias and Reboita 2021; Collazo et al. 2022; Gulizia et al. 2022; de Medeiros et al. 2022; Reboita et al. 2022; Olmo et al. 2022a). Fewer studies have focused on the atmospheric circulation and moisture transport (Barros and Doyle 2018; Sierra et al. 2018, 2021; Flores-Aqueveque et al. 2020; Olmo et al. 2022b; Valencia and Mejía 2022; Agudelo et al. 2023; Arias et al. 2023; Bazzanela et al. 2024; Correa et al. 2024; Zhang et al. 2024) or land–atmosphere interactions (Baker et al. 2021; Baker and Spracklen 2022).

As in other continental regions, major climate biases in global models result from coarse spatial resolutions or missing physical processes, particularly in areas with complex topography. Finer-scale climate modeling partially solves these biases, and is also necessary for various applications, such as basin-scale hydrological research or local climate impact assessments, many of which rely on global climate simulations as boundary conditions. Given the limitations in climate model simulations for South America, this study aims to evaluate the performance of GCMs and Earth System Models (ESMs) participating in the sixth phase of the Coupled Model Intercomparison Project (CMIP6), to simulate the key large-scale features controlling climate in South America. The focus is on specific circulation patterns and the transport of moisture and heat through the continental boundaries of South America. Hence, this work is intended to facilitate the selection of climate models to be used as boundary conditions for regional simulations in this continent. In particular, we aim to provide a model ranking according to their performance in simulating the different features and spatial fields considered. We do not aim to discuss the mechanisms behind the different model biases; however, their identification and characterization may also support future research in understanding the causes of these biases. Similar works have been developed for Europe and Africa (Brandt et al. 2013; Pinto et al. 2018).

2 Data and methodology

2.1 Reanalysis data

We used monthly fields of precipitation, sea level pressure (SLP), and SST, as well as horizontal winds (zonal and meridional components), pressure velocity (omega), and specific humidity at different pressure levels from the ERA5 reanalysis (Hersbach et al. 2020) for the period 1979–2014. ERA5 is the most recent state-of-the-art reanalysis of the European Center for Medium-Range Weather Forecasts (ECMWF), with a 0.25° horizontal grid size and 137 pressure levels. This reanalysis has been previously used as a reference dataset to evaluate the performance of CMIP6 models in South America (e.g. Arias et al. 2021b; Ortega et al. 2021; Bazzanela et al. 2024; Olmo et al. 2022b; Zhang et al. 2024). ERA5 data is accessible at https://www.ecmwf.int/en/forecasts/datasets/reanalysis-datasets/era5.

2.2 CMIP6 simulations

This work also uses model outputs for monthly fields of horizontal winds, omega and specific humidity at different pressure levels, as well as SLP, SST, and precipitation from 57 CMIP6 models (Table A1 of the Supplementary Material). We considered historical runs during the period 1980–2014 for comparison with the ERA5 reanalysis. Historical simulations include all forcing observed during 1850–2014, including changes in the atmospheric composition due to anthropogenic forcing (greenhouse gas emissions due to fossil fuel burning and land use, anthropogenic aerosol emissions) and natural forcing (volcanic eruptions, solar variability, internal variability; Eyring et al. 2016). CMIP6 outputs are available from the Earth System Grid Federation archives (https://esgf-node.llnl.gov/search/cmip6).

2.3 Spatial patterns of winds, SLP, SST, and precipitation

We estimated the seasonal mean and annual biases of the CMIP6 models in simulating horizontal winds, SLP, SST and precipitation. In addition, we use Taylor diagrams (Taylor 2001) to evaluate the performance of the climate models reproducing the seasonal and annual spatial patterns of these variables. These diagrams allow for the assessment of model performance by comparing the spatial correlation, standard deviation and root mean square error (RMSE) of the model simulation with respect to a reference dataset (ERA5 in our case). The models with a better performance exhibit higher correlation coefficients

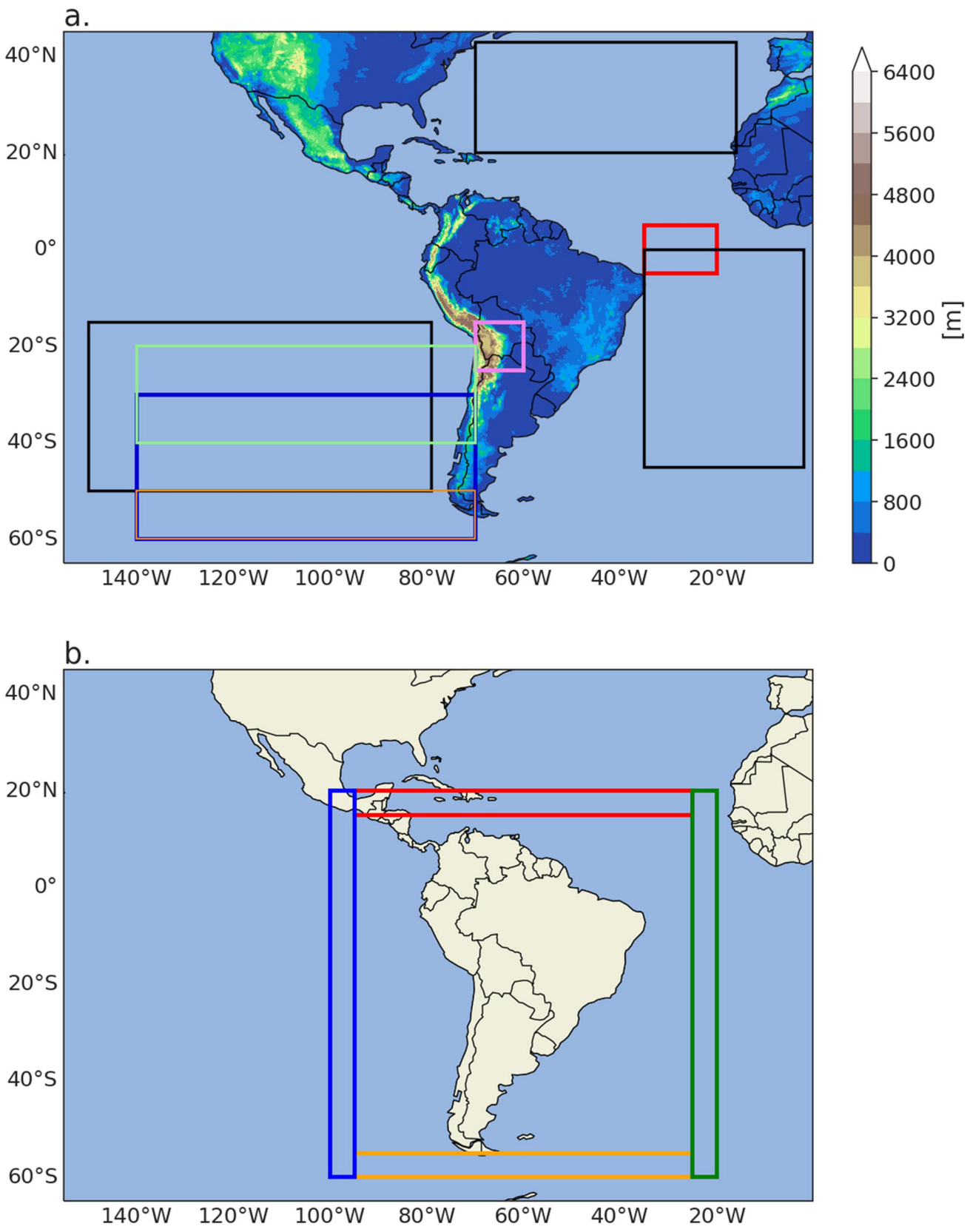
a.
40°N
20°N
0°
20°S
40°S
60°S
140°W
120°W
100°W
80°W
60°W
40°W
20°W
6400
5600
4800
4000
3200
2400
1600
800
0
[m]
b.
40°N
20°N
0°
20°S
40°S
60°S
140°W
120°W
100°W
80°W
60°W
40°W
20°W

◂**Fig. 1** **a** Domains used to compute atmospheric circulation indices: Atlantic Trade Winds (ATW; red rectangle), the Southeastern Pacific Westerlies (SPW; blue), the Bolivian High (BH; purple), the Southern Hemisphere Subtropical Jet (SHSJ; green), the Southern Hemisphere Polar Jet (SHPJ; orange), and the Subtropical Highs (black). Color shades indicate ERA5 topography. **b** Zonal and meridional boundaries used to compute Vertically Integrated Moisture Flux and Vertically Integrated Energy Flux across the South American domain

(i.e. closer to 1), standard deviation ratios close to 1 (i.e. the simulated variance is close to the ERA5 variance) and low RMSE (i.e. close to 0). The statistics involved in the Taylor diagrams for each particular model were computed at the original model resolution. This methodology has been previously used in the evaluation of climate model simulations over South America (e.g. Yin et al. 2013; Sierra et al. 2015; Arias et al. 2021b; Ortega et al. 2021; Olmo et al. 2022a, b; Bazzanela et al. 2024).

Regarding atmospheric circulation, we look at specific features that matter for continental climate. At low levels, we compute indices to quantify the Atlantic Trade Winds (ATW) and Southeastern Pacific Westerlies (SPW). For ATW, the index is computed as the 850 hPa zonal wind average over the domain 5° S–5° N, 35–20° W (see Fig. 1a). Note that this index is defined as positive for an easterly flow. For SPW, we compute two indices based on the 850 hPa zonal wind in the region 140°–70° W, 30°–60° S (Fig. 1a). A first index corresponds to the Westerlies latitudinal location (i.e. the latitude of the maximum flow within the SPW domain). The second index is the Westerlies strength (i.e. the domain-average flow).

Regarding the upper-level circulation, we considered an index for the BH, computed as the domain average of the DJF 200 hPa geopotential height anomalies over the region 15º–25º S, 60º–70º W (see Fig. 1a), according to Reason (2016). In addition, we evaluated the modeled Southern Hemisphere Subtropical Jet (SHSJ) using the 200 hPa zonal wind speed over the region 140°–70° W, 20º S–40º S (see Fig. 1a). Similarly, we used the 200 hPa zonal wind speed over the region 140°–70° W, 50º–60º S to evaluate the Southern Hemisphere Polar Jet (SHPJ; see Fig. 1a). As for the SPW, we compute two indices for the SHSJ and SHPJ measuring the latitudinal location (i.e. the latitude of the maximum flow) and strength (i.e. the domain-average flow).

To further evaluate the model performance in simulating SST phenomena affecting the South American climate, we computed the ENSO power spectrum for each model, by estimating the Fourier transform of SST anomalies (SSTAs) averaged over the Niño3.4 region. Moreover, we evaluated how the CMIP6 models reproduce the spatial pattern of DJF SSTAs over the Pacific surrounding South America during ENSO warm phases (El Niño).

2.4 Regional Hadley and Walker cells

We also evaluated the performance of the CMIP6 models in simulating the Hadley and Walker cells over the South American domain. To do this, we followed the approach proposed by Zhang and Wang (2013), based on a regional mass streamfunction (Ψ) estimate without violating the principle of negligible net transport of zonal mass. This approach uses the meridional component of the irrotational flow, which contributes to the vertical motion in the north–south circulation represented by the Hadley cell. We calculated the meridional mass streamfunction of the regional Hadley circulation for each latitude over tropical South America, as shown by Eq. 1:

$$\psi = \frac{2\pi\cos\theta}{g}\int_0^p \left[V_{IR}\right]dp \tag{1}$$

where θ is the latitude, g is the gravitational acceleration, p is pressure, and $\left[V_{IR}\right]$ is the irrotational component of the meridional wind averaged for the longitudes 70º–50º W.

For the regional Walker cell, we used the zonal component of the irrotational flow that contributes to vertical motion in the east–west circulation associated with this cell and it is computed for the 150º–20º W longitudinal band. The irrotational component of the zonal wind was averaged over the latitudes between 5º S and 5º N.

2.5 Subtropical highs

To evaluate the simulation of the subtropical high pressure centers in the surrounding oceans, we used SLP for the regions: 50°–69° W, 50°–15° S to represent the South Pacific Subtropical High (SPSH); 80°–10° W, 45°–20° N for the North Atlantic Subtropical High (NASH); and 45° W–10° E, 45°S–0° for the South Atlantic Subtropical High (SASH) (see Fig. 1a). Therefore, we defined three indices for each subtropical high: latitudinal location (latitude of the maximum SLP within the specific domain), longitudinal location (longitude of the maximum SLP within the specific domain), and intensity (maximum SLP within the specific domain).

2.6 Water and energy fluxes across boundaries

Boundary conditions are key in the development of regional simulations, in particular the lateral fluxes of water and energy across the boundaries of the regional domain. Therefore we evaluated the simulation of vertically integrated fluxes of moisture and heat. The

Vertically Integrated Moisture Flux (VIMF) across the boundaries of the South American domain was estimated by Eq. 2:

$$VIMF = \frac{1}{g}\int_{pl}^{pu} v_h q dp \tag{2}$$

where v_h is the horizontal wind component normal to the boundary of interest (zonal for the latitudinal boundaries or meridional for the longitudinal boundaries), *pu* is pressure in the upper level, *pl* is pressure in the lower level, and *q* is specific humidity. The vertical integration was performed between 1000 and 100 hPa. Therefore, we analyzed the VIMF transects across the different boundaries (Fig. 1b). We also evaluated the vertical structure of the moisture fluxes (*qu, qv*) along these boundaries, where *u* and *v* are the zonal and meridional wind components.

Similarly, the Vertically Integrated Heat Flux (VIHF) across the boundaries of the South American domain was estimated using Eq. 3 (Peixoto and Oort 1992):

$$VIHF = \frac{1}{g}\int_{pl}^{pu} v_h s dp \tag{3}$$

$$s = C_p T + \phi \tag{4}$$

where *pu* is pressure in the upper level, *pl* is pressure in the lower level, v_h is the horizontal wind component normal to the boundary of interest (zonal for the latitudinal boundaries or meridional for the longitudinal boundaries), *s* is the dry static energy (DSE), C_p is the specific heat capacity of dry air at constant pressure, *T* is temperature, and ϕ is geopotential (*gz*). As for the VIMF, the vertical integration was performed between 1000 and 100 hPa. As for the VIMF, we evaluated the VIHF transects across the different boundaries (Fig. 1b). We also evaluated the vertical structure of the heat fluxes (*Tu, Tv*) along these boundaries.

In summary, we analyzed four types of features: (i) horizontal patterns of winds (850 hPa, 200 hPa), SLP, SST, and precipitation over the entire South American continent and adjacent oceans; (ii) indices related with circulation features (ATW, SPW, BH, SHSJ, SHPJ, Subtropical Highs, ENSO); (iii) spatial patterns of regional circulation cells (Hadley and Walker cells); and (iv) moisture and heat fluxes across the continental boundaries (shown in Fig. 1b). All the indices and spatial patterns are estimated for the 1980–2014 period to match the availability of ERA5 data and CMIP6 historical simulations.

2.7 Model evaluation

To evaluate the performance of the different models, we considered two approaches. First, we used the Taylor Skill Score (*TS*) to rank the models according to their performance in the simulation of the spatial patterns of 850 hPa wind speeds, 200 hPa wind speeds, SLP, SST, El Niño SSTA, precipitation, regional Walker circulation, regional Hadley circulation, and the vertical structure of moisture and heat fluxes through the domain boundaries. This metric is based on the Taylor diagrams by considering the model performance in the Pearson correlation coefficient and the standard deviation with respect to the reference dataset (ERA5) for each spatial field. The *TS* is computed as indicated by Eq. 5 (Hirota and Takayabu 2013):

$$TS = \frac{(1+R)^4}{4 * \left(\sigma_m/\sigma_o + \sigma_0/\sigma_m\right)^2} \tag{5}$$

where R is the correlation coefficient between the simulated (model) and the reference (ERA5) spatial field, and σ_o and σ_m correspond to the standard deviations of the reference and simulated spatial fields, respectively.

Second, to rank the models according to their performance in simulating particular features of the regional circulation (e.g. ATW, SPW, BH, SHSJ, SHPJ, NASH, SPSH, SASH and ENSO power spectrum) as well as the heat and moisture fluxes across the continental boundaries, we estimated a Ranking Score (*RS*) using the correlation coefficient and the RMSE between the indexes obtained for each model and the ERA5 data. For this second approach, we scored the models according to their ranking for each feature, following a simple metric, as shown by Eq. 6:

$$RS = \frac{\left(N - R_k + 1\right)}{N} \tag{6}$$

where N is the number of models used and R_k is the model rank for a particular feature. For the correlation coefficient, the rank R_k is estimated by arranging models in descending order according to their correlation coefficient with ERA5, assigning a R_k value that ranges from 1 (model with the higher correlation coefficient) to N (model with the lower correlation coefficient). For the RMSE, the rank R_k is estimated arranging models in ascending order according to their RMSE with ERA5, assigning a R_k value that ranges from 1 (model with the lower RMSE) to N (model with the higher RMSE). Thus a *RS* equal to 1 indicates the model with the best performance in that particular feature. *RS* values closer to zero indicate a poor model performance. Please note that N depends on the feature considered since not all models have available outputs for all the variables.

3 Mean regional atmospheric circulation simulated by the CMIP6 models

We considered the main atmospheric circulation features affecting the South American domain. In particular, we assessed how the models represent the low-level circulation depicted by the 850 hPa wind field, the ATW and the SPW in the surroundings of South America. For the upper level circulation, we considered the 200 hPa winds in the same domain, as well as the BH, SHSJ and SHPJ.

3.1 Low-level circulation

Figure 2 shows how the CMIP6 models simulate the 850 hPa horizontal winds in the domain 140°–0° W, 60° S–40° N. Models exhibit a better performance in representing low-level winds over this domain during DJF and SON, when there is less spread among models but also higher correlations with the ERA5 reference dataset; however, correlation coefficients are above 0.8 during MAM and JJA, indicating a good performance by the models (Fig. 2a–d). In general, the multimodel ensemble shows a better performance than individual models, as it locates closer to the reference data in the Taylor Diagrams. The multimodel ensemble captures the mean seasonal low-level circulation in the continent, with a clear representation of the Trade Winds and the extratropical Westerlies (Fig. 2e–h). The multimodel ensemble shows a clear change in the direction of the Trade Winds over the Caribbean Sea, with a northerly direction during DJF and a southerly direction during JJA, and increased intensity during DJF and JJA. The Westerlies depicted by the ensemble

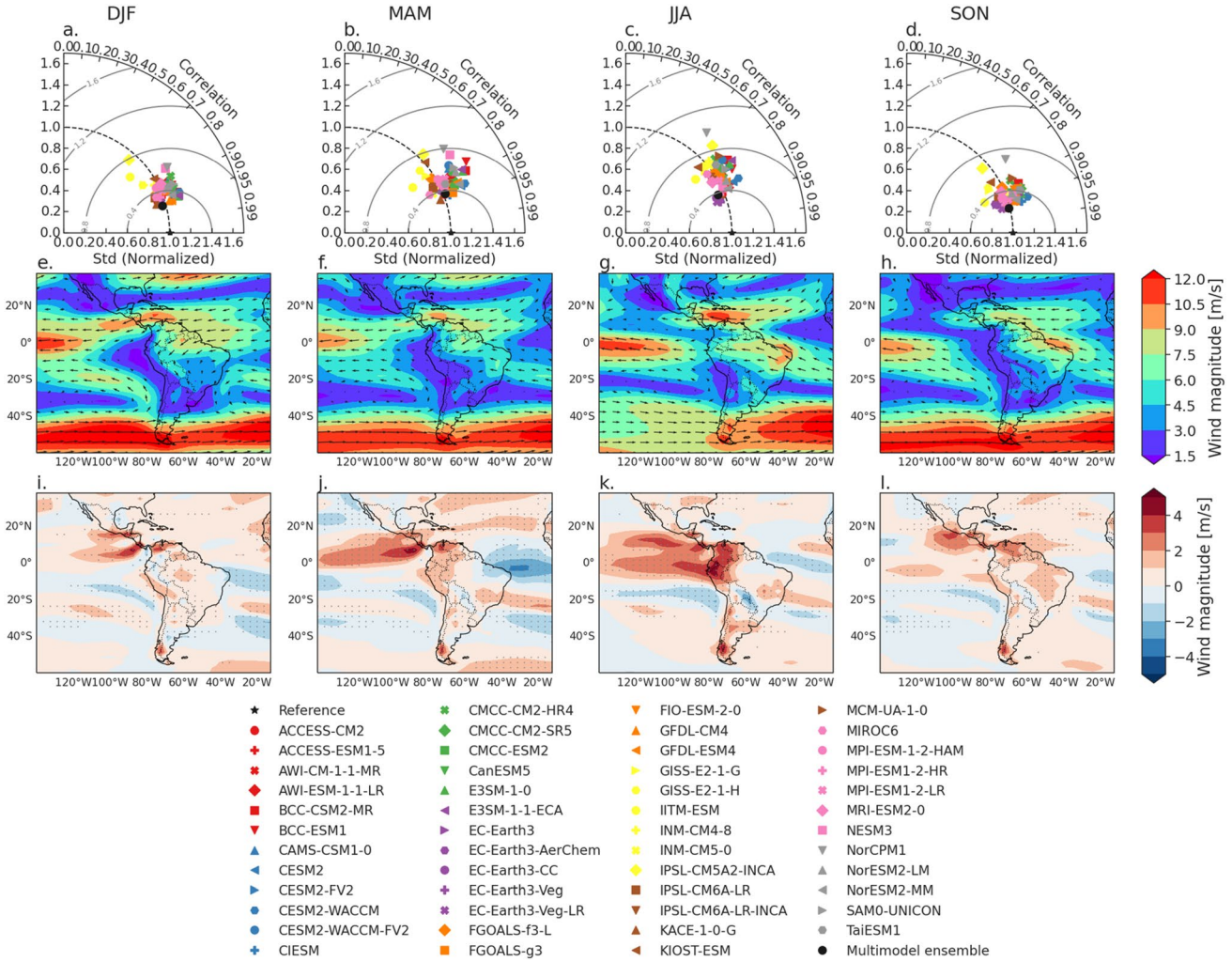

Fig. 2 **a–d** Seasonal Taylor diagrams of the 850 hPa horizontal wind speed over the 140°–0° W, 60° S–40° N domain. **e–h** Multimodel seasonal mean 850 hPa horizontal winds (vectors) and wind speed (shades). **i–l** Multimodel seasonal mean biases of the 850 hPa horizontal wind speed. Dots indicate when at least 80% of the CMIP6 models agree on the sign of the multimodel mean bias. Reference data corresponds to ERA5 reanalysis

mean show intensification during the austral spring (SON) and summer (DJF). The ensemble mean bias indicates that models overestimate the 850 hPa wind speed over the north Atlantic ocean, the tropical Pacific, the Caribbean Sea, and most of the South American continent, particularly the northwest and the southernmost portions (Fig. 2i–l). This latter feature may be related with the reduced elevation of the Andes in most of the evaluated models. By contrast, there is high agreement in their underestimation of low-level wind velocities over the tropical and subtropical Atlantic Ocean, central South America (Bolivia and Paraguay), and the southeastern Pacific (around 20º S).

3.1.1 Atlantic trade winds

Since the main South America domain considered in Fig. 2 includes different circulation patterns, we examine some particular aspects of the low-level circulation in the region. First, we evaluated the ATW, a key climate driver for tropical South America. Figure 3 shows the annual cycle of the Trade Wind index defined in the ATW region

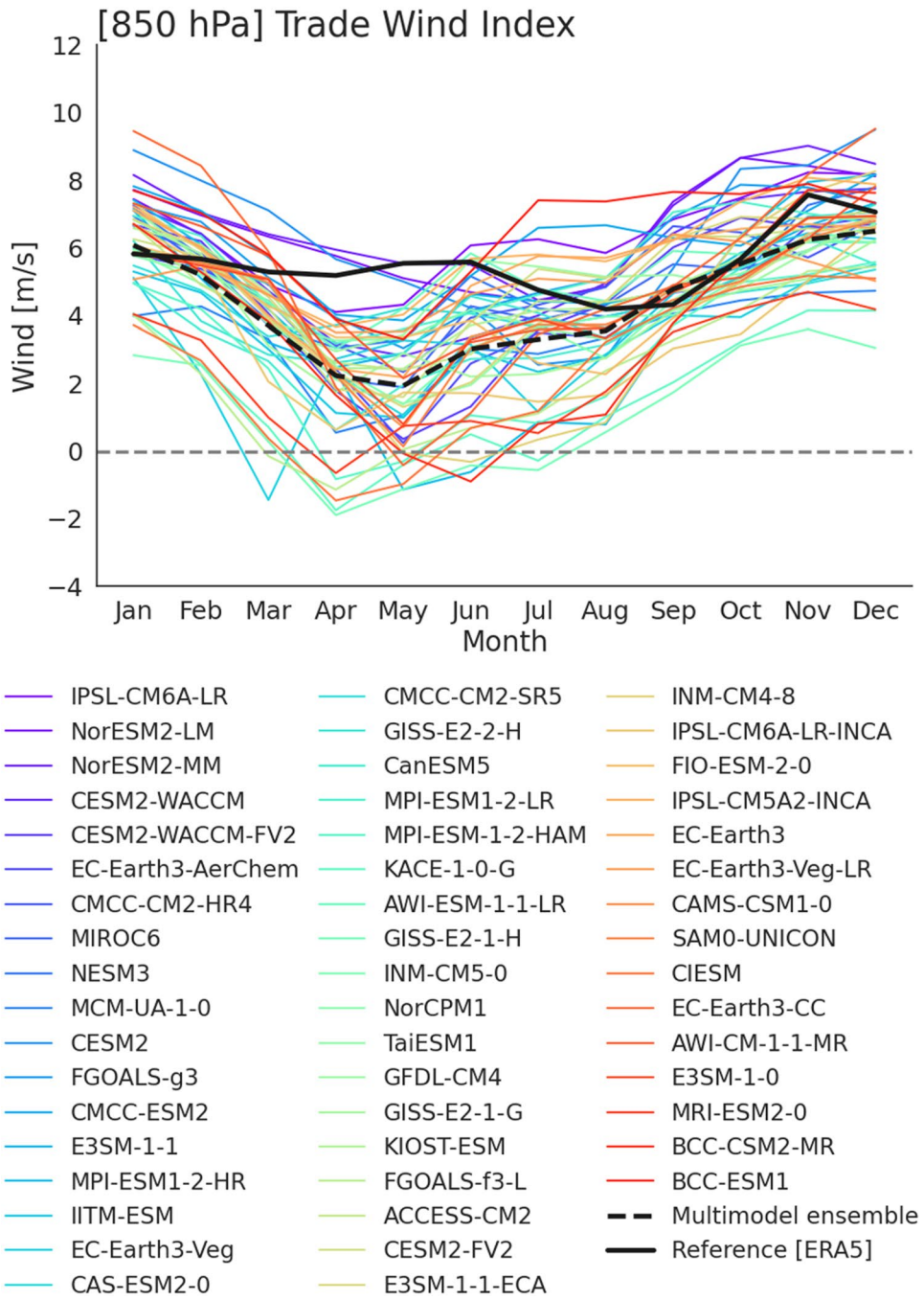

Fig. 3 Climatological annual cycle of the Atlantic Trade Wind index (see Fig. 1a) for the different CMIP6 models available and the reference ERA5 dataset (thick black line). For comparison, the ensemble mean is shown (thick dotted black line). Negative values represent a westerly flow. The dotted line indicates the zero line (i.e. the Trade winds change from easterly (positive index) to westerly (negative index)

(Sect. 2.3.1) based on the reference ERA5 dataset and the CMIP6 models. According to ERA5, there is a strengthening of the Trade Winds during November, and a second minor peak in May–June, within an overall weak seasonal cycle. In general, CMIP6 models show a consistent mean magnitude but greater seasonal amplitude of the Trade Winds. The modeled Trade Winds strengthen during September-January, with the largest values around November, as suggested by ERA5. However, the models show a clear minimum by April–May, which is not observed in ERA5, where the weakest Trade Winds are shown around August. Even more, a few models show negative values of the Trade Wind index, indicating a change in the direction of these winds (becoming westerly) mainly during March-June. This result suggests that the CMIP6 models have systematic difficulties reproducing the annual cycle of the Trade Winds affecting South America, particularly due to negative biases during March-June. This is also observed from the multimodel ensemble.

3.1.2 Southeastern Pacific westerlies

Another important feature of the low-level circulation in South America are the SPW, which control the hydroclimate variability of the extratropical regions of the continent. Figure 4a shows the annual cycle of the mean Westerlies strength (Sect. 2.3.1), according to ERA5 and the CMIP6 models. The CMIP6 models show a better agreement with ERA5 in their representation of the SPW strength than for the Trade Winds, the agreement is clearer when considering the multimodel ensemble (Fig. 4a).

The SPW index exhibits a unimodal annual cycle with minimum values during the austral winter (May–August) and stronger winds during the summer (November-March). Although this annual cycle is well represented by the models, the magnitude exhibits an important spread, with variations of about 5 m/s among models. In contrast to the mean strength, the mean location of these winds is not well represented by many of the models (Fig. 4b). According to ERA5, the SPW exhibit their southernmost location during June–August at latitude around 60º S. However, many models show a northward shift in the location of this wind belt during austral winter, with locations as far north as 35º–45º S. We note that the westerly flow and the related mid-latitude storm track in the Southeastern Pacific are better defined and peak in summer, while during winter, the westerly flow band is wider and extends northward, with a less distinct maximum within a large latitudinal range from about 30–60° S. This less distinct maximum flow may explain sudden jumps in the detection of the latitude of maximum wind, as shown by some models during the winter.

3.2 Upper-level circulation

Regarding the upper-level circulation, Fig. 5 shows the model performance for the seasonal 200 hPa wind fields over the domain 140º–0º W, 60º S–40º N. The Taylor diagrams suggest that the models show a better resemblance with respect to ERA5 during JJA and SON, when the symbols corresponding to the models are located closer to the reference data (Fig. 5a–d). For DJF and MAM, the models exhibit larger standard deviations and lower correlations than for the other seasons, although correlation coefficients are above 0.8 during all seasons (Fig. 5a–d). In general, the multimodel ensemble outperforms individual models, as detected from the Taylor Diagrams. The ensemble mean 200 hPa wind field (Fig. 5e–h) shows the clear development of the subtropical jet over the Southern Hemisphere (30º–60º S), with stronger velocities during JJA and SON (Fig. 5e–h). The ensemble mean also suggests an anticyclonic circulation over the South American Altiplano in DJF, consistently with the development of the BH. The ensemble mean bias of the 200 hPa wind magnitude (Fig. 5i–l) indicates that models overestimate 200 hPa wind velocity over northern South America during the entire year, and show the stronger overestimates in the Amazon during JJA and SON, and southern South America during SON. Also, CMIP6 models overestimate the velocities associated with the Subtropical Jet over the southeastern Pacific and underestimate the velocity of the 200 hPa winds over the Altiplano and the south tropical eastern Pacific during DJF and MAM. All these biases have a high agreement among models, indicating that they are common biases among the CMIP6 models.

3.2.1 Bolivian high

Figure 5 considers a large domain that mixes important regional circulation patterns for the continent. Because the BH is a dominant feature of the upper-level circulation in South America during the austral summer, we show the annual cycle of the BH index (defined in Sect. 2.3.1; Fig. 6). In general, the models exhibit an annual cycle that resembles that from ERA5, with larger 200 hPa geopotential heights in DJF and smaller heights in JJA, in agreement with the establishment of an upper-level anticyclone during the austral summer over the Altiplano region in association with the development of the SAMS. However, most of the models underestimate the BH index with respect to ERA5, showing 200 hPa geopotential heights up to 200 m below the ERA5 estimate. This is clearly observed in the multimodel ensemble.

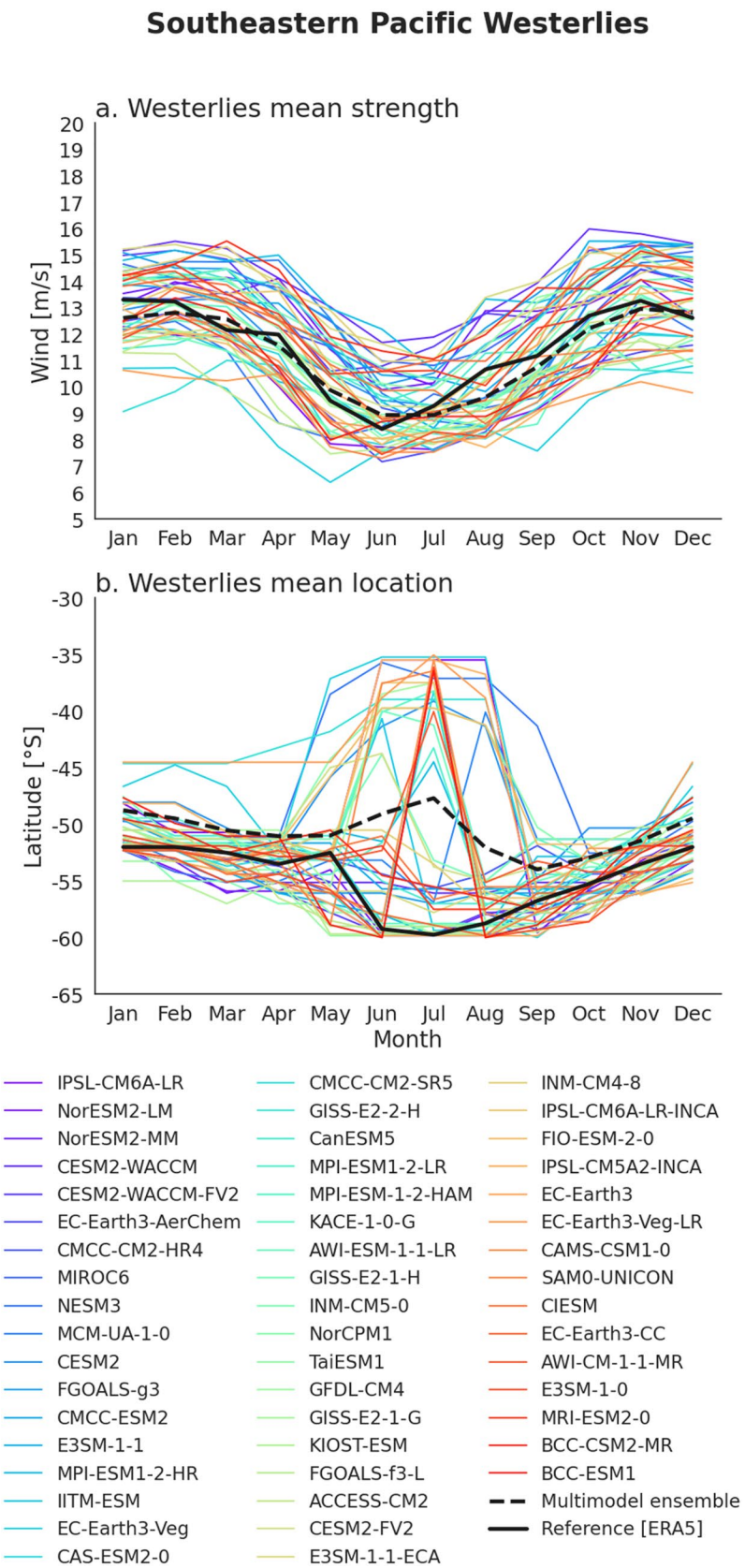

Fig. 4 Climatological annual cycle of the **a** strength and **b** mean latitudinal location of the South Pacific Westerlies (see Fig. 1a) for the different CMIP6 models available and the reference ERA5 dataset (thick black line). For comparison, the ensemble mean is shown (thick dotted black line)

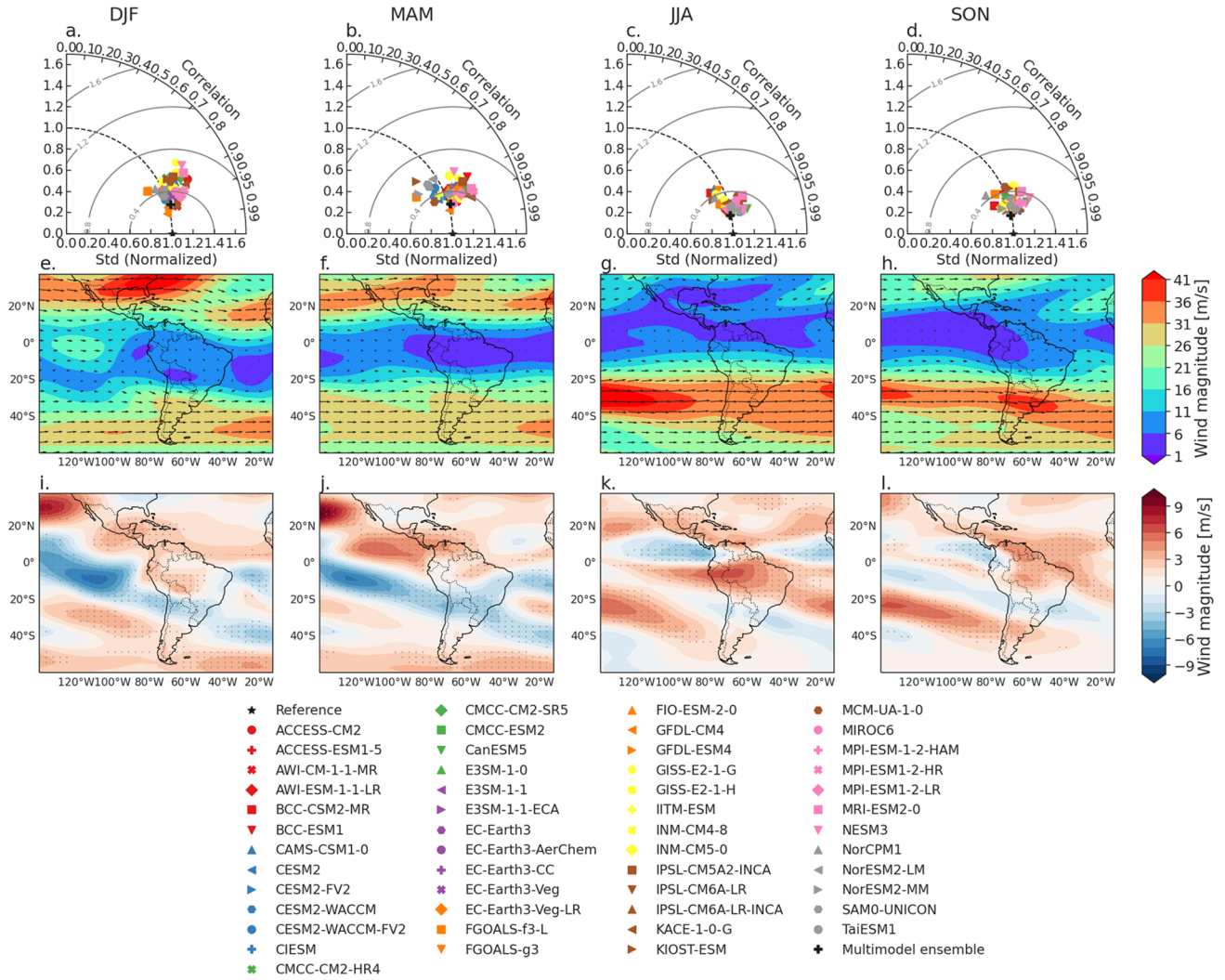

Fig. 5 **a**–**d** Seasonal Taylor diagrams of the 200 hPa horizontal wind speed over the 140°–0° W, 60° S–40° N domain. **e**–**h** Multimodel seasonal mean 200 hPa horizontal winds (vectors) and wind speed (shades). **i**–**l** Multimodel seasonal mean biases of the 200 hPa horizontal wind speed. Dots indicate when at least 80% of the CMIP6 models agree on the sign of the multimodel mean bias. Reference data corresponds to ERA5 reanalysis

3.2.2 Subtropical and polar jet streams

Another important feature of the upper-level circulation in South America are the Subtropical and Polar Jets. Figure 7a shows the annual cycle of the mean strength of the SHSJ indicating that the models capture the unimodal annual cycle of this upper-level circulation, with stronger 200 hPa winds during June–September and weaker velocities in November-March. The models exhibit a larger spread during the season of a stronger SHSJ, with mean velocities varying between 30 and 50 m/s (for comparison, the mean strength from ERA5 for July–August is about 38 m/s). Regarding the mean latitudinal location of the SHSJ Fig. 7b), models also exhibit a good resemblance in comparison to ERA5, showing a northward displacement of the jet during August–November (with a location about 30° S) and a southward migration by December–April (with a location about 38° S). The multimodel ensemble shows a better simulation of the SHSJ mean location than its mean strength (Fig. 6a, b).

Regarding the SHPJ, Fig. 7c, d indicate that the models generally capture the mean annual cycle of the jet intensity, with two maxima in February–March and October–December, and one stronger minimum in May–June. In contrast with the SHSJ, many models fail in reproducing the mean latitudinal location of the SHPJ, although the multimodel ensemble shows a best performance in this annual cycle, exhibiting is southernmost location in September–November, as suggested by ERA5 (Fig. 7d).

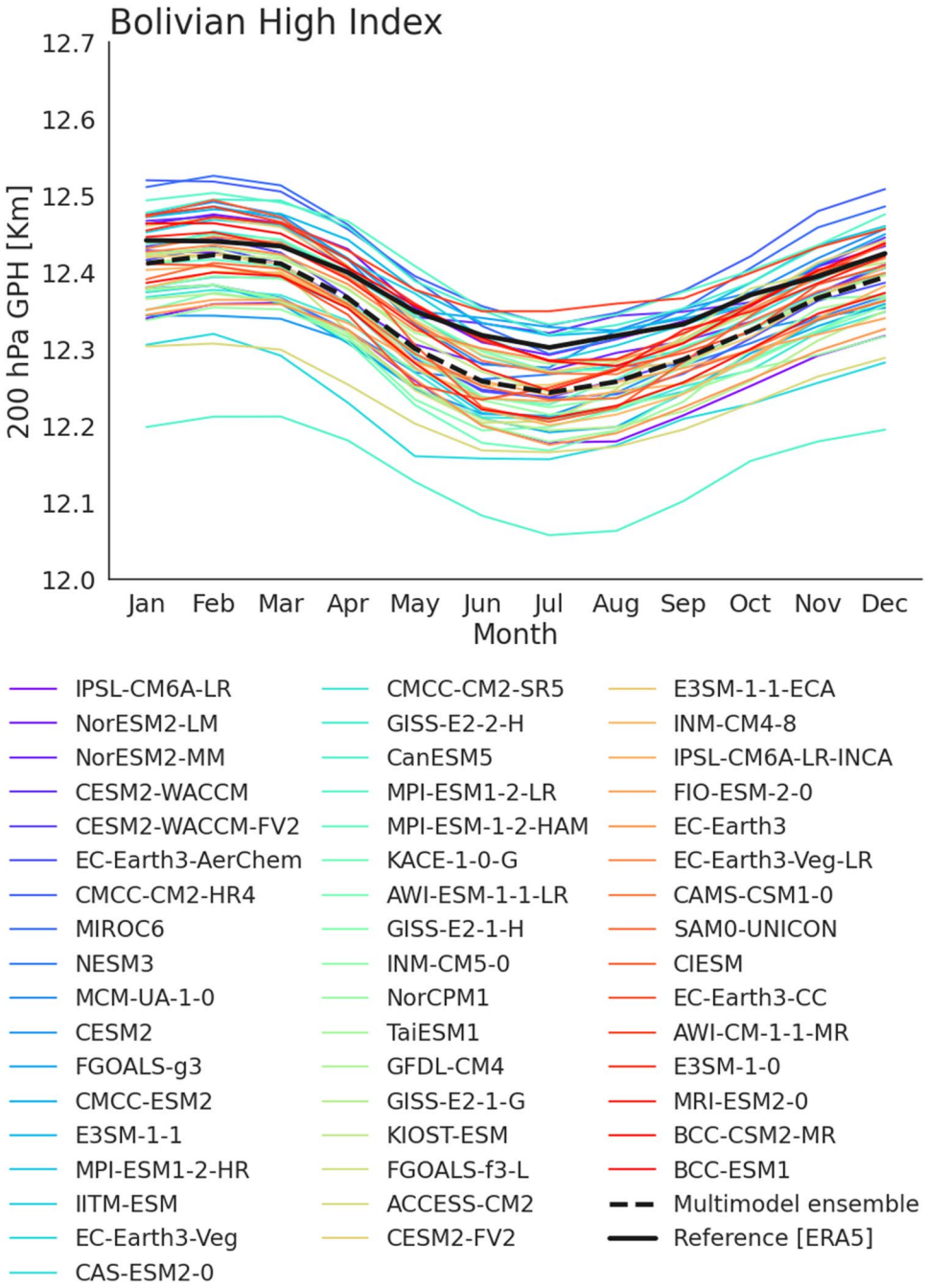

Fig. 6 Climatological annual cycle of the Bolivian High index (see Fig. 1a) for the different CMIP6 models available and the reference ERA5 dataset (thick black line). For comparison, the ensemble mean is shown (thick dotted black line)

3.3 Regional circulation cells

Up to this point, we have evaluated the ability of the CMIP6 models in representing the horizontal atmospheric circulation over South America and its surroundings. In this section, we assess how these models simulate the main regional circulation cells in South America: the Walker and Hadley cells.

3.3.1 Walker circulation

Figure 8 summarizes the performance of the set of CMIP6 models in representing the mean seasonal regional Walker circulation, depicted by the irrotational component of the zonal wind for the 150° W–20° W longitudinal band, averaged over the latitudes between 5° S and 5° N (see Sect. 2.3.2). It is clear that models have more difficulties

in the simulation of the South American Walker cell (Fig. 8a–d) than for the 850 hPa and 200 hPa wind fields (Figs. 2a–d and 5a–d). The models exhibit a better performance of the Walker cell during SON and DJF. For MAM and JJA, CMIP6 models show more variations in their standard deviation and much lower correlation values with respect to ERA5 (Fig. 8a–d). The multimodel ensemble does not necessarily outperform individual models, with some of them exhibiting a better performance in the Taylor Diagrams.

CMIP6 models show a weaker irrotational component of the zonal wind for both positive and negative values (note that the ensemble mean values (Fig. 8e–h) and the ensemble mean bias (Fig. 8i–l) have opposite signs for the four seasons, especially in MAM and JJA, when the model agreement is higher). This suggests that the CMIP6 models underestimate the strength of the regional Walker cell in South America throughout the year, in comparison to ERA5.

3.3.2 Hadley circulation

Figure 9 shows the model performance in simulating the mean seasonal regional Hadley cell, according to the mass streamfunction averaged over the longitudes 70º W–50º W (see Sect. 2.3.2). As also detected for the Walker cell, the models better simulate the seasonal horizontal wind fields than the South American Hadley cell. The CMIP6 models show a higher skill in their simulation of the regional Hadley cell for DJF while the worst performance is observed for SON (Fig. 9a–d). As also observed for the Walker circulation, some individual models show a better performance than the multimodel ensemble.

The multimodel ensemble captures the characteristic seasonal cycle of the Hadley cell over South America: ascending motion centered about 15º–20º S during austral summer and a northward migration until reaching its northernmost location (around 20º–40º N) in boreal summer (Fig. 9e–h). The ensemble mean bias suggests a dipole centered about 5º N, with positive values to the south and negative values to the north, particularly in DJF and MAM, detected in at least 80% of the models considered (Fig. 9–l). This indicates that the CMIP6 models overestimate the ascending motion over south tropical South America (between 20º and 10º S) in austral summer (DJF) and fall (MAM), while the ascending motion over north tropical South America (around 5º N) is underestimated during boreal summer (JJA) and fall (SON).

3.4 Subtropical highs in the adjacent oceans

The subtropical highs over the Atlantic and Pacific oceans are among the boundary conditions influencing regional atmospheric circulation in South America. In particular, features such as the Atlantic Trade Winds and the Westerlies are associated with the anticyclonic circulation of these subtropical highs. As a first approach, Fig. 10 shows the model performance in the simulation of the seasonal patterns of SLP over the 140º–0º W, 60º S–40º N domain. In general, CMIP6 models show a similar performance in their simulation of SLP fields during the different seasons (Fig. 10a–d), exhibiting a better performance than for the regional cells (Figs. 8a–d and 9a–d). The multimodel ensemble shows a better performance than most of individual models as it locates closer to the reference data in the Taylor Diagrams.

The multimodel mean shows the high SLP patterns over the North Atlantic, the South Pacific and the South Atlantic, characteristic of the NASH, SPSH, and SASH, respectively, with a strengthened NASH in boreal winter/spring and enhanced SPSH and SASH in austral winter/spring (Fig. 10e–h). It also shows the lower pressures over the tropical region throughout the year and over the SAMS core region during the austral summer. The mean biases indicate that the CMIP6 models underestimate SLP over most of western South America, particularly over the western Amazon during SON and Peru and northern Chile during the entire year, in association with underestimated SPSH SLP (Fig. 10i–l). In contrast, the models overestimate the SLP over the NASH and SASH centers during the different seasons.

For a more detailed analysis of the subtropical highs, Supplementary Fig. A1 shows the annual cycle of the intensity, latitudinal location and longitudinal location of the three anticyclonic systems. The CMIP6 models generally resemble the annual cycle of the anticyclone intensity and the latitudinal location of the three subtropical highs, exhibiting greater intensities for the Atlantic anticyclones than for the SPSH, as also shown in Fig. 10e–h. The model spread in the subtropical high intensity is about 6–8 hPa for the SASH, 8–10 hPa for the SPSH and 8–12 hPa for the NASH (Supplementary Fig. A1a–c).

The unimodal cycle of the latitudinal location of the anticyclones is well captured by some of the models, mainly for the SASH and SPSH, showing more northward (southward) locations for the SASH and SPSH during February-May (JJA) and for the NASH during July–September (April–May) (Supplementary Fig. A1d–f). Among the three anticyclones, the NASH latitudinal location has more differences between the models, with variations up to 10º of latitude, and with some models exhibiting a biased annual cycle. The annual cycle of the longitudinal location of the anticyclone center exhibits more differences for the SASH, with models exhibiting large shifts throughout the year in comparison to ERA5 (Supplementary Fig. A1g). For the other anticyclones, the models show an annual cycle more in agreement with ERA5. In general, the models have more difficulties simulating the longitudinal location of the

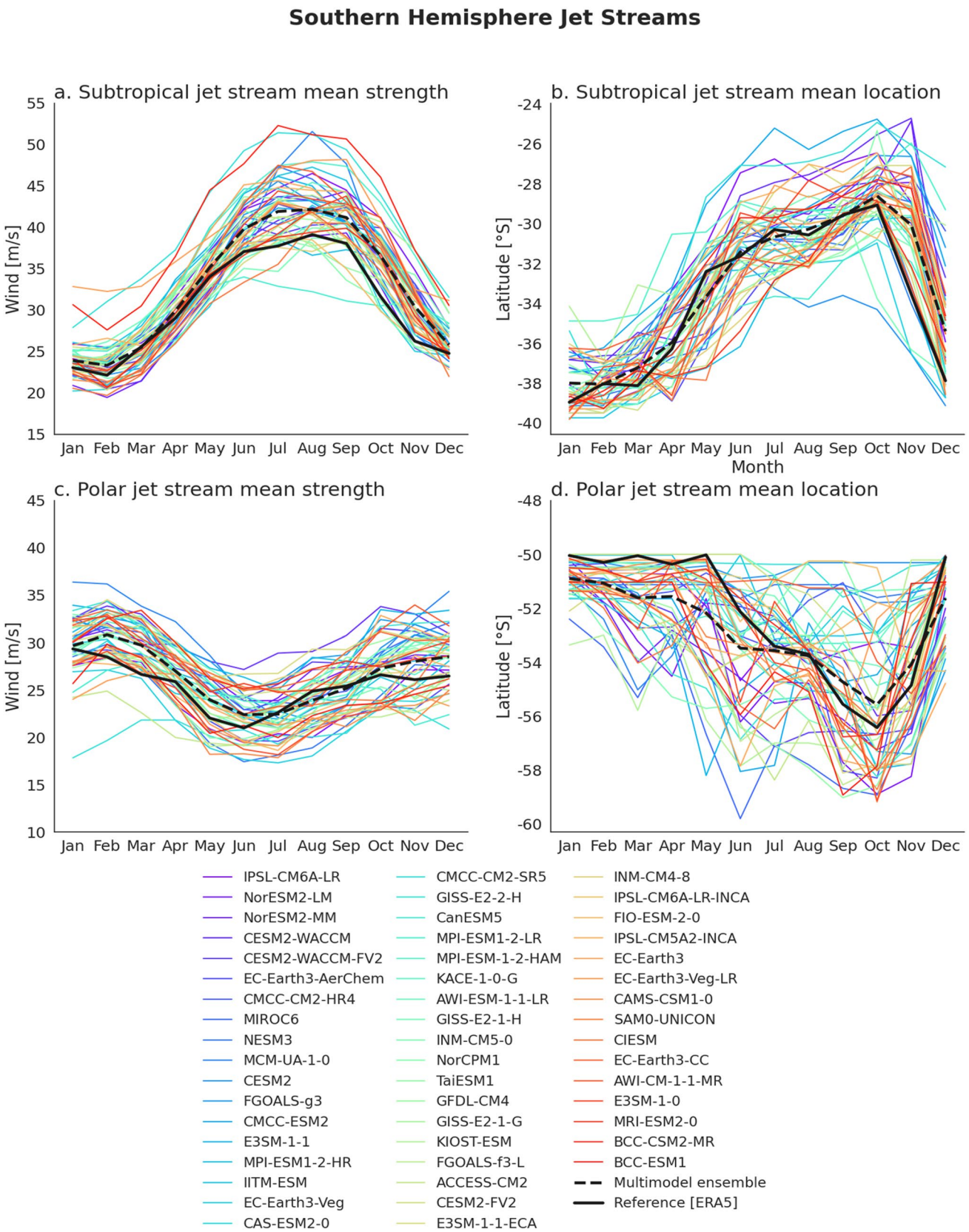
Southern Hemisphere Jet Streams
a. Subtropical jet stream mean strength
Wind [m/s]
b. Subtropical jet stream mean location
Latitude [°S]
Month
c. Polar jet stream mean strength
Wind [m/s]
d. Polar jet stream mean location
Latitude [°S]
Jan Feb Mar Apr May Jun Jul Aug Sep Oct Nov Dec
IPSL-CM6A-LR
NorESM2-LM
NorESM2-MM
CESM2-WACCM
CESM2-WACCM-FV2
EC-Earth3-AerChem
CMCC-CM2-HR4
MIROC6
NESM3
MCM-UA-1-0
CESM2
FGOALS-g3
CMCC-ESM2
E3SM-1-1
MPI-ESM1-2-HR
IITM-ESM
EC-Earth3-Veg
CAS-ESM2-0
CMCC-CM2-SR5
GISS-E2-2-H
CanESM5
MPI-ESM1-2-LR
MPI-ESM-1-2-HAM
KACE-1-0-G
AWI-ESM-1-1-LR
GISS-E2-1-H
INM-CM5-0
NorCPM1
TaiESM1
GFDL-CM4
GISS-E2-1-G
KIOST-ESM
FGOALS-f3-L
ACCESS-CM2
CESM2-FV2
E3SM-1-1-ECA
INM-CM4-8
IPSL-CM6A-LR-INCA
FIO-ESM-2-0
IPSL-CM5A2-INCA
EC-Earth3
EC-Earth3-Veg-LR
CAMS-CSM1-0
SAM0-UNICON
CIESM
EC-Earth3-CC
AWI-CM-1-1-MR
E3SM-1-0
MRI-ESM2-0
BCC-CSM2-MR
BCC-ESM1
Multimodel ensemble
Reference [ERA5]

◂**Fig. 7** Climatological annual cycle of the **a** strength and **b** mean latitudinal location of the Southern Hemisphere Subtropical Jet, and the **c** strength and **d** mean latitudinal location of the Southern Hemisphere Polar Jet over South America (see Fig. 1a) for the different CMIP6 models available and the reference ERA5 dataset (thick black line). For comparison, the ensemble mean is shown (thick dotted black line)

anticyclonic core over the three oceans, particularly for the SASH (Supplementary Fig. A1g–i).

3.5 Sea surface temperatures in the adjacent oceans

Among the most relevant boundary conditions influencing the South American atmospheric circulation are the SSTs in the surrounding oceans. Figure 11 shows the performance of the CMIP6 models in simulating the seasonal SSTs in the 140°–0° W, 60° S–40° N domain. In ERA5, SST conditions are provided by existing level-4 (i.e., gapless) gridded datasets. The ERA5 SST product considers

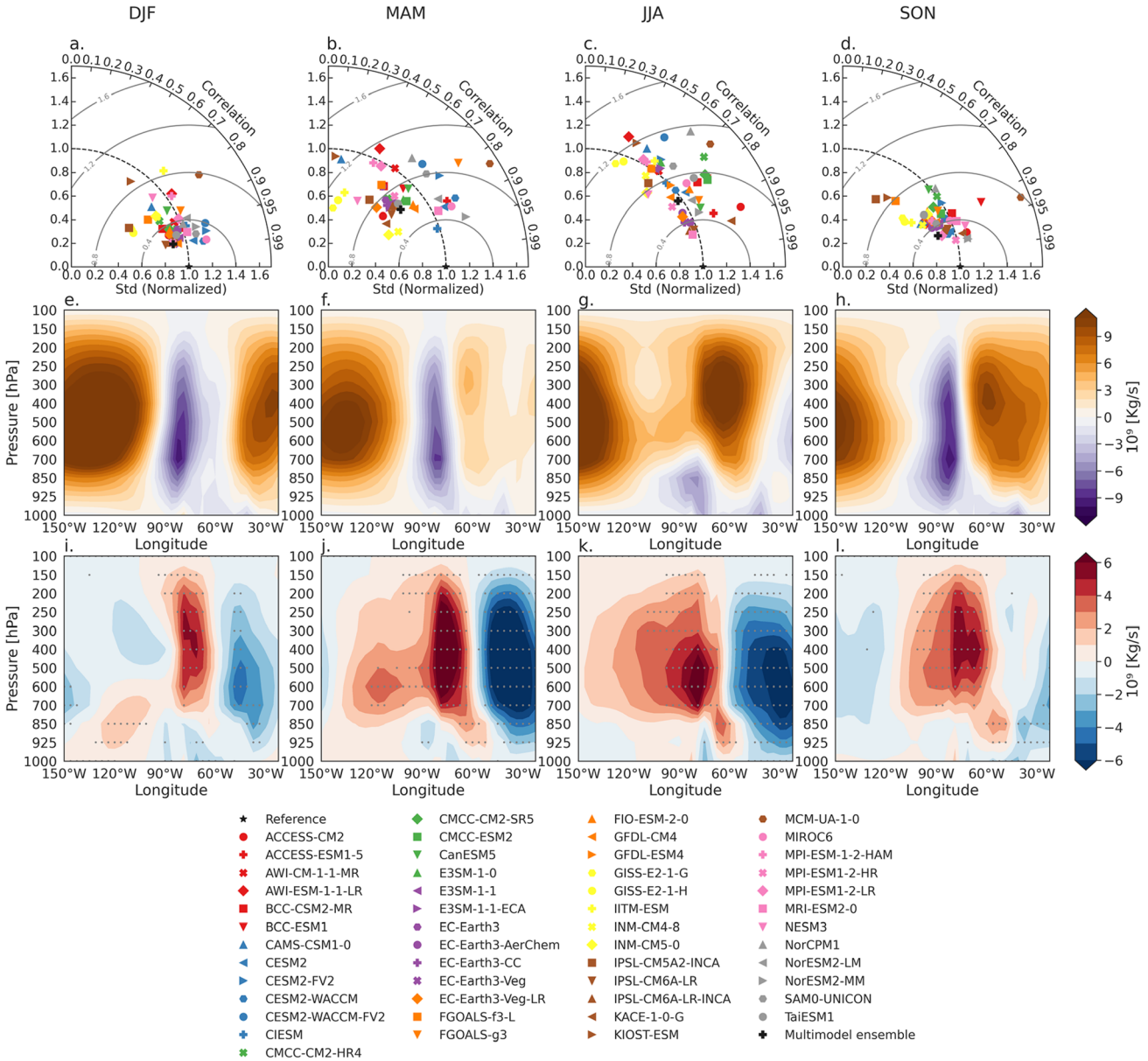

Fig. 8 **a**–**d** Seasonal Taylor diagrams of the irrotational component of the zonal wind for the 150°–20° W longitudinal band, as a representation of the regional Walker Cell in South America. The irrotational component of the zonal wind is averaged over the latitudes between 5° S and 5° N. **e**–**h** Multimodel seasonal mean irrotational component of the zonal wind for South America. i)-l) Multimodel seasonal mean bias of the irrotational component of the zonal wind for South America. Dots indicate when at least 80% of the models agree on the sign of the multimodel mean bias. Reference data corresponds to ERA5 reanalysis

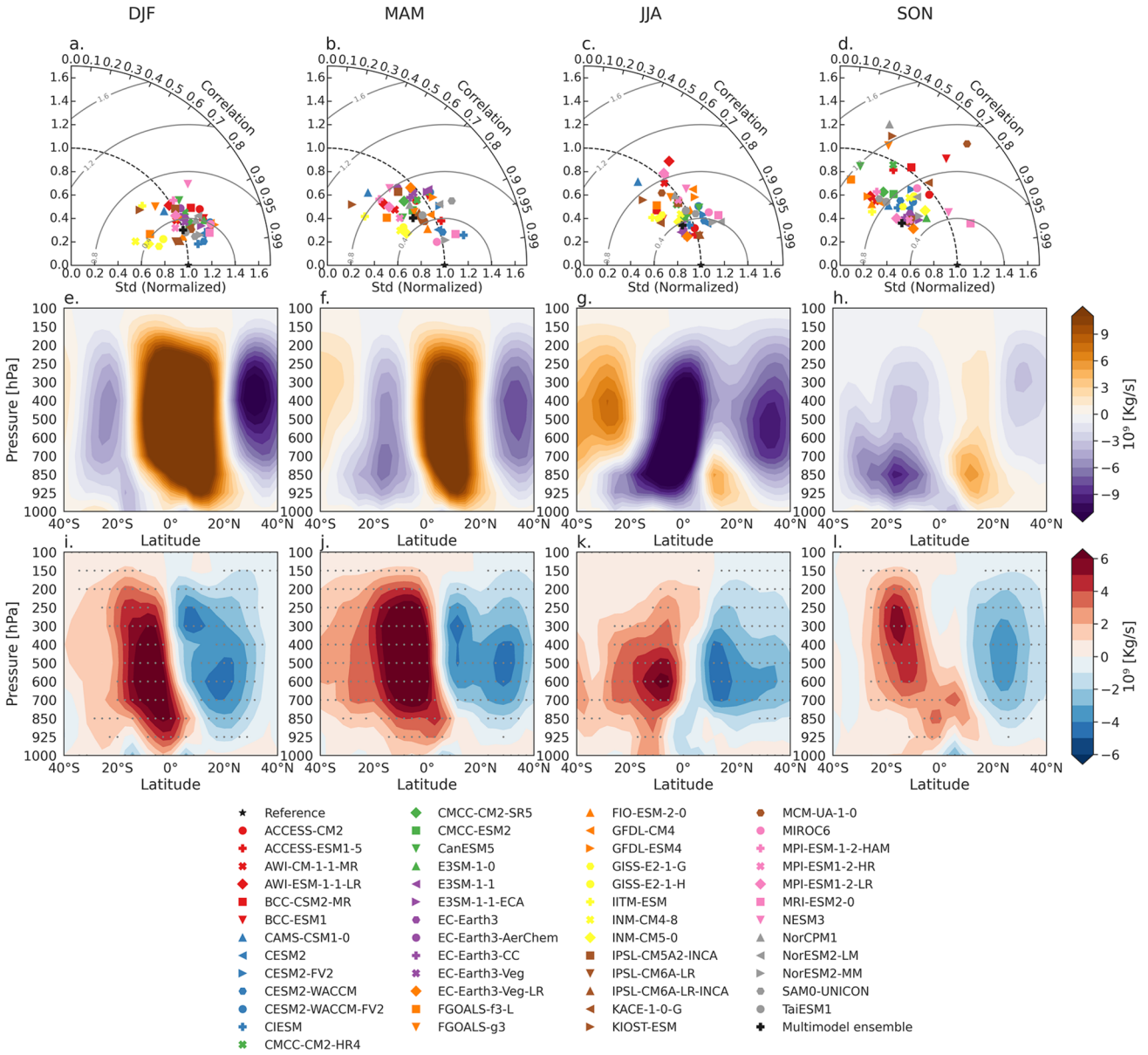

Fig. 9 **a–d** Seasonal Taylor diagrams of the regional meridional mass streamfunction (Eq. 1) averaged over the longitudes 70º–50º W, as a representation of the regional Hadley Cell in South America. e)-h) Multimodel seasonal mean regional meridional mass streamfunction for South America. Positive (negative) values indicate clockwise (counterclockwise) vertical rotation. **i–l** Multimodel mean bias of the mean regional meridional mass streamfunction for South America. Dots indicate when at least 80% of the models agree on the sign of the multimodel mean bias. Reference data corresponds to ERA5 reanalysis

various flavors of the Met Office Hadley Centre HadISST2 product as well as the Climate Change Initiative SST v1.1, which are combined with the Met Office OSTIA product used in the ECMWF medium-range forecasting system since 2007 (Hersbach et al. 2020). This means that ERA5 assimilates multiple observational products. Moreover, we compared ERA5 SST data with two observational datasets (COBESST2 and ERSSTv5). In particular, we evaluated the power spectrum of the Oceanic El Niño Index (ONI) reproduced by all datasets and ERA5 captures the peak spectrum about 3–5 years, as the other datasets (not shown). Also, we compared the probability density function (PDF) of the seasonal SST spatial fields over the 140º–0º W, 60º S-40º N domain (i.e. oceans surrounding South America) and found that ERA5 exhibits a PDF remarkably close to the observational datasets during all seasons (not shown). Hence we considered ERA5 as the reference dataset to evaluate model performance in simulating SSTs over the adjacent oceans of South America.

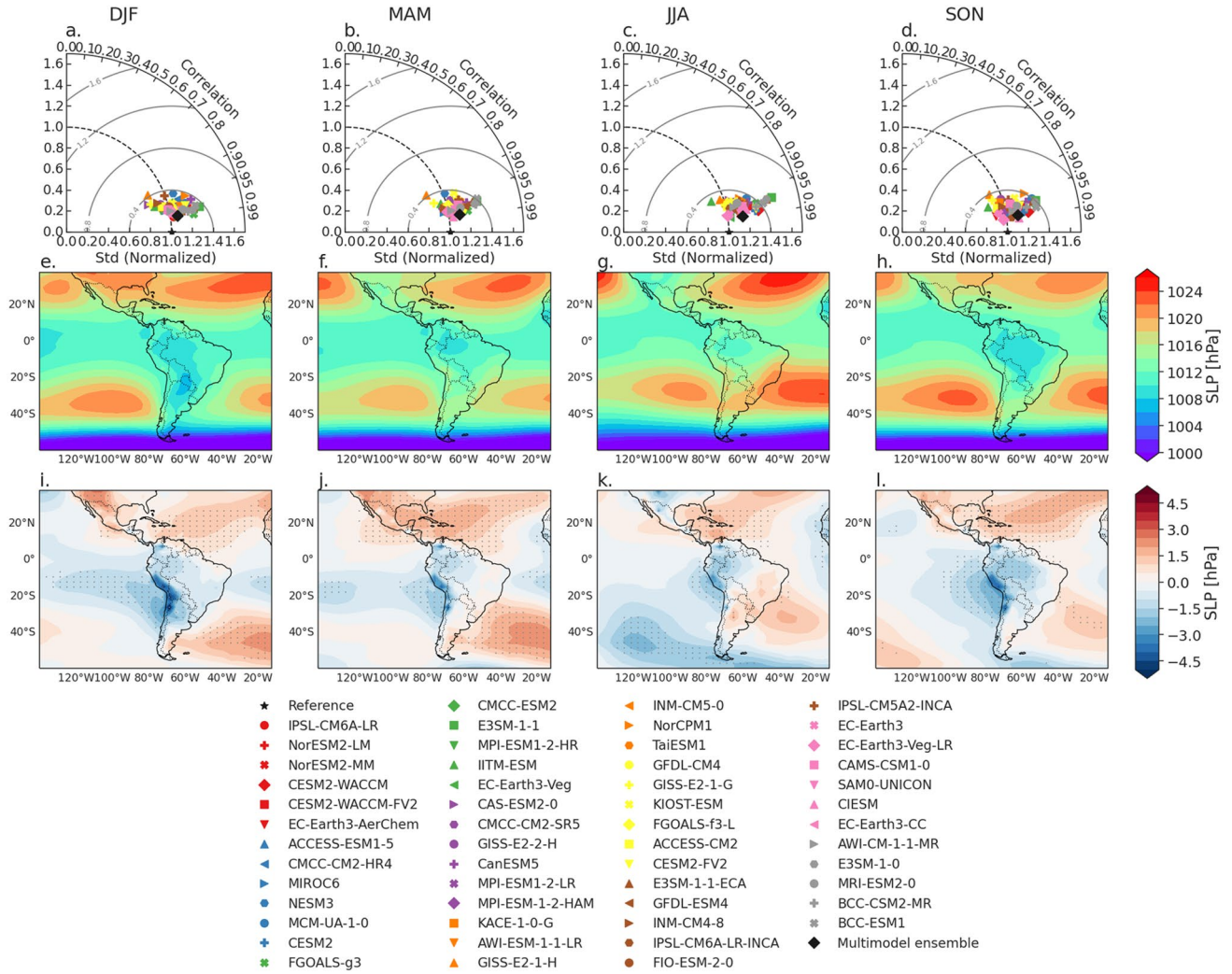

Fig. 10 **a**–**d** Seasonal Taylor diagrams of the sea level pressure (SLP) over the 140°–0° W, 60° S–40° N domain. **e**–**h** Multimodel seasonal mean SLP. **i**–**l** Multimodel seasonal mean biases of the SLP. Dots indicate when at least 80% of the CMIP6 models agree on the sign of the multimodel mean bias. Reference data corresponds to ERA5 reanalysis

Among all the variables considered in our study, seasonal SSTs are the field in which the CMIP6 models exhibit the best performance, in terms of the standard deviation and correlations of the spatial patterns (Fig. 11a–d). The only exception is the E3SM-1–0 model, which shows very low correlation coefficients with respect to the reference data, biasing the multimodel ensemble. CMIP6 models resemble the regional SST patterns, with a cold tongue over the eastern tropical Pacific and warmer conditions in the northwestern Atlantic/Caribbean warm pool (Fig. 11e–h). The ensemble mean bias shows that CMIP6 models underestimate SSTs over the north Atlantic ocean and Caribbean Sea and overestimate them over the Pacific ocean surrounding South America, particularly in the cold tongue, during the entire year (Fig. 11i–l). The models also overestimate the SSTs over the extratropical oceans of South America.

ENSO is one of the most important SST features influencing South American climate [see Cai et al. (2020) for a detailed review of the main impacts of ENSO in South America]. Supplementary Fig. A2 shows how the CMIP6 models simulate the SSTAs pattern associated with El Niño. These models are able to capture the positive SSTAs over the tropical eastern Pacific in association with El Niño (Supplementary Fig. A2a). However, the spatial correlation between the DJF SSTAs pattern between the models and the ERA5 reference dataset is low (some models show correlation coefficients as low as 0.3; Supplementary Fig. A2b). Also, there is a large spread in the standard deviation of the SSTA pattern of the models with respect to ERA5 (Supplementary Fig. A2b). The power spectrum of the Niño3.4 index suggests that many models underestimate the dominant ENSO frequency with respect to ERA5: while

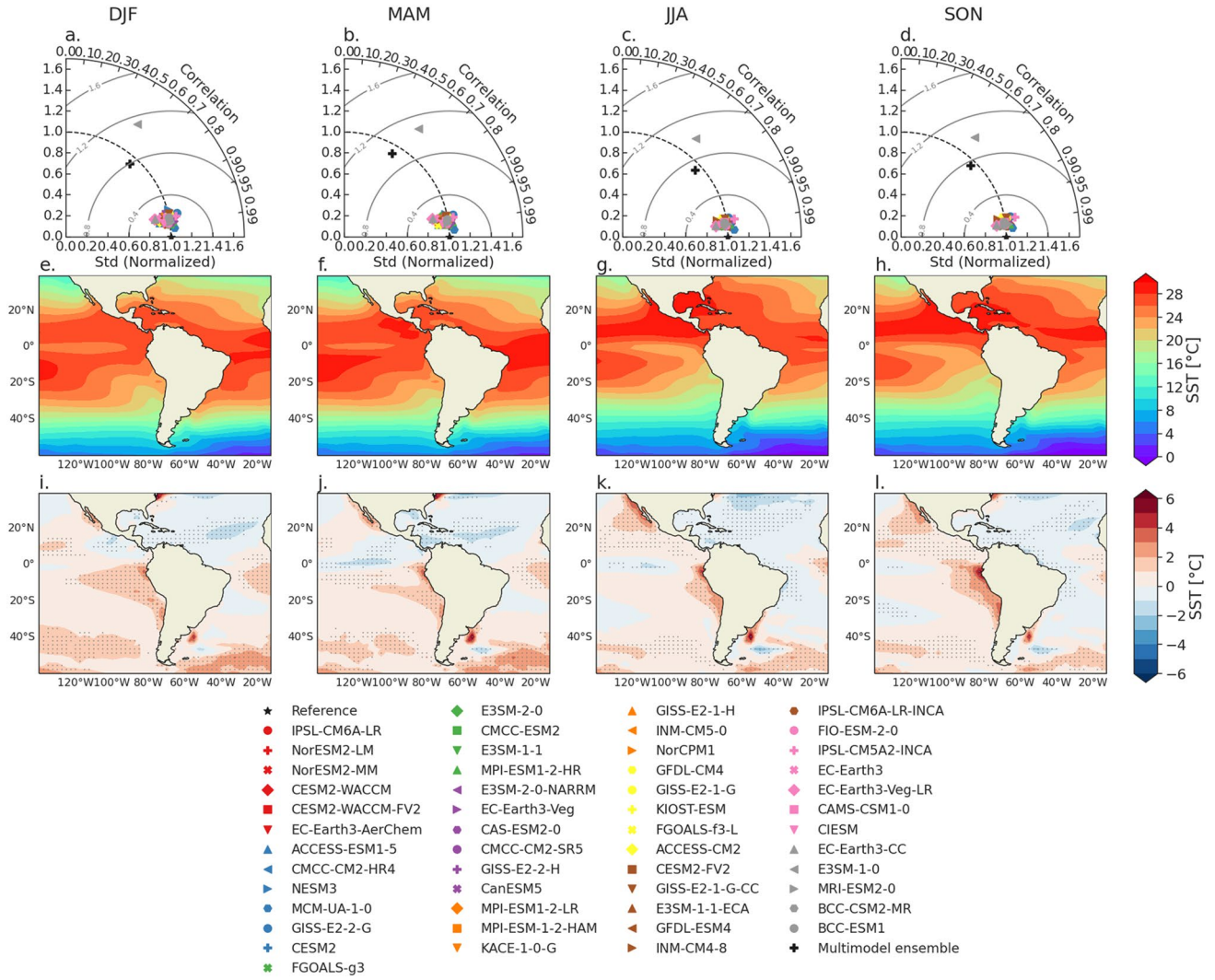

Fig. 11 **a–d** Seasonal Taylor diagrams of the sea surface temperature (SST) over the adjacent oceans of South America (140º–0º W, 60º S–40º N). **e–h** Multimodel seasonal mean SSTs over the adjacent oceans of South America. **i–l** Multimodel seasonal mean biases of the SSTs. Dots indicate when at least 80% of the CMIP6 models agree on the sign of the multimodel mean bias. Reference data corresponds to ERA5 reanalysis

ERA5 shows a dominant frequency of 4–5 years, many of the CMIP6 models have a spectral peak around 2–3 years (Supplementary Fig. A2c). In contrast, a second set of models show longer ENSO frequencies of more than 5 years.

3.6 Precipitation

Although the main goal of this paper is not focused on the evaluation of seasonal precipitation in South America, the model performance for this variable is an important input to assess how well these models simulate regional climate in South America. Thus Fig. 12 shows the performance of the CMIP6 models in simulating the seasonal precipitation in the 80º–40º W, 60º S–15º N domain. This domain focuses on the South American landmass in order to evaluate model performance in simulating precipitation over the continent. The CMIP6 models better simulate regional precipitation during JJA than during the other seasons (Fig. 12a–d). As observed for other variables, the multimodel ensemble generally outperforms individual models when analyzing Taylor Diagrams. In general, the CMIP6 models capture the wettest and driest regions over the continent as well as the seasonal precipitation patterns, however the ensemble mean shows the double ITCZ bias during DJF and MAM (Fig. 12e–h). The ensemble mean bias indicates strong biases over the oceanic ITCZ, with overestimations (underestimations) with respect to the reference dataset over the north (south) equatorial ITCZ, showing a high agreement among models (Fig. 12i–l). Over the continent, there is agreement in an overestimation of seasonal precipitation over northern and

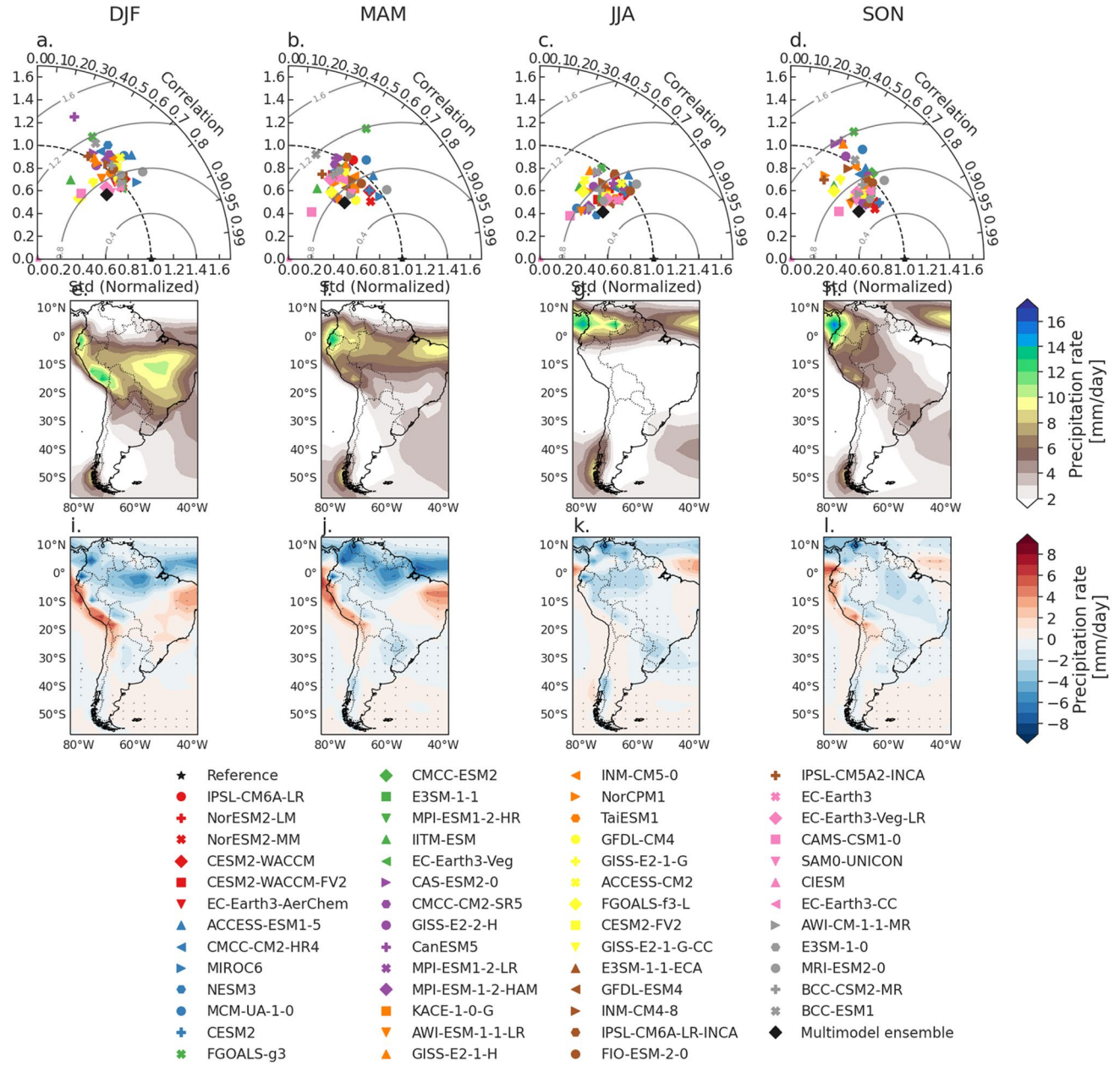

Fig. 12 **a–d** Taylor diagrams of the seasonal mean precipitation over the domain 80º–40º W, 60º S–15º N. **e–h** Multimodel seasonal mean precipitation over South America. **i–l** Multimodel mean biases of precipitation over South America. Dots indicate when at least 80% of the models agree on the sign of the multimodel mean bias. The reference data is the ERA5 reanalysis

southern South America and underestimation over northeastern Brazil and the western side of the Andes over Ecuador, Peru and Bolivia (Fig. 12i–l). The analysis over a larger domain (the domain shown in Fig. 10 and other figures) yields to similar conclusions (not shown).

4 Water and energy fluxes across the continental boundaries simulated by the CMIP6 models

Section 3 discusses how the CMIP6 models reproduce different circulation features in South America, which may play an important role in regional simulations forced by GCMs. In this section, we focused on the vertically integrated moisture and heat fluxes across the South American boundaries,

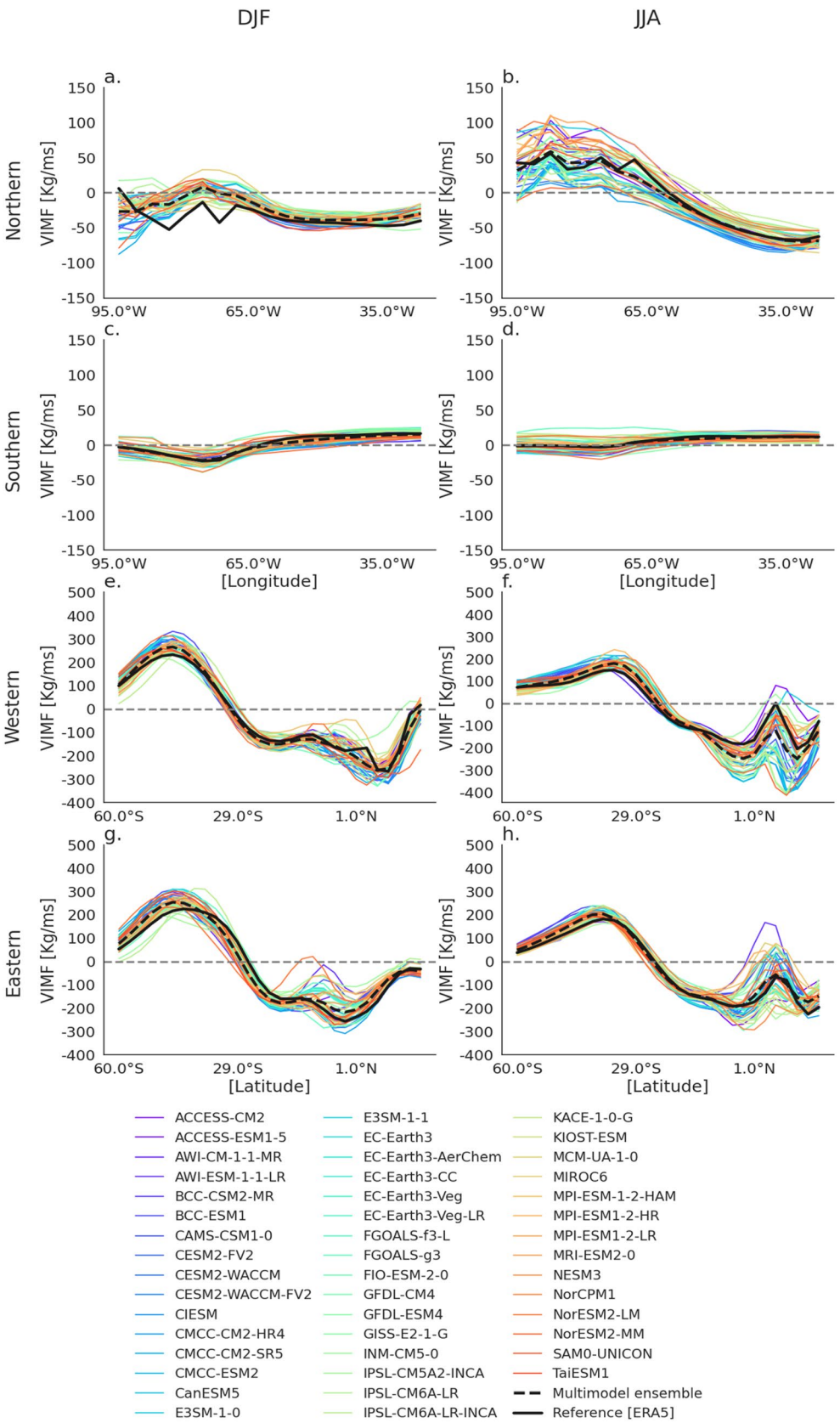
DJF
JJA
a.
b.
c.
d.
e.
f.
g.
h.
Northern
Southern
Western
Eastern
VIMF [Kg/ms]
150
100
50
0
-50
-100
-150
95.0°W
65.0°W
35.0°W
[Longitude]
500
400
300
200
-200
-300
-400
60.0°S
29.0°S
1.0°N
[Latitude]
ACCESS-CM2
ACCESS-ESM1-5
AWI-CM-1-1-MR
AWI-ESM-1-1-LR
BCC-CSM2-MR
BCC-ESM1
CAMS-CSM1-0
CESM2-FV2
CESM2-WACCM
CESM2-WACCM-FV2
CIESM
CMCC-CM2-HR4
CMCC-CM2-SR5
CMCC-ESM2
CanESM5
E3SM-1-0
E3SM-1-1
EC-Earth3
EC-Earth3-AerChem
EC-Earth3-CC
EC-Earth3-Veg
EC-Earth3-Veg-LR
FGOALS-f3-L
FGOALS-g3
FIO-ESM-2-0
GFDL-CM4
GFDL-ESM4
GISS-E2-1-G
INM-CM5-0
IPSL-CM5A2-INCA
IPSL-CM6A-LR
IPSL-CM6A-LR-INCA
KACE-1-0-G
KIOST-ESM
MCM-UA-1-0
MIROC6
MPI-ESM-1-2-HAM
MPI-ESM1-2-HR
MPI-ESM1-2-LR
MRI-ESM2-0
NESM3
NorCPM1
NorESM2-LM
NorESM2-MM
SAM0-UNICON
TaiESM1
Multimodel ensemble
Reference [ERA5]

◂**Fig. 13** Climatological Vertically Integrated Moisture Flux (VIMF; Eq. 2) across the **a**, **b** northern, **c**, **d** southern, **e**, **f** western, and **g**, **h** eastern boundaries of the South American domain (see Fig. 1b) for December-February (DJF) and June–August (JJA) for the different CMIP6 models available and the reference ERA5 dataset (thick black line). For comparison, the multimodel ensemble is shown (thick dotted black line)

as they provide key boundary conditions for these types of simulations.

4.1 Vertically integrated moisture fluxes

The VIMF transects across the South American boundaries (Fig. 1b) for the DJF and JJA seasons are presented in Fig. 13. In general, the CMIP6 models capture the pattern of meridional (Fig. 13a–d) and zonal (Fig. 13e–h) VIMF across the continental boundaries. The multimodel ensemble mean captures the VIMF transect across the four boundaries considered. This is also observed in the Taylor diagrams of the DJF vertical moisture fluxes (Supplementary Figs. A3a–d), clearly showing that the models show a higher skill in their simulation of the zonal fluxes across the eastern and western boundaries (Supplementary Fig. A3c, d). The northern VIMF has a peak around 80º W-70º W while the southern VIMF is more uniform across the zonal boundaries, which are well represented by the models (Fig. 13a–d). The northern VIMF is stronger during JJA (Fig. 13a, b) while the southern VIMF does not show much change between DJF and JJA; however, the model spread is larger for DJF (Figs. 13c, d).

The models show a larger spread when simulating the zonal VIMF peaks over the tropical latitudes (25º S and equator; Fig. 13e–h). The multimodel mean shows that the zonal fluxes have larger magnitudes than the meridional fluxes (Supplementary Fig. A3e–h), with larger biases for the zonal and southward fluxes (Figs. 13 and Supplementary FigA3i–l). As expected, the moisture fluxes are much larger at the lower levels of the troposphere (Supplementary Fig. A3e–h). Furthermore, the ensemble mean of the northerly vapor flux over the northern boundary seems to be weaker than in ERA5, especially along the Caribbean Sea (Fig. 13a and Supplementary Fig. A3i). Over the western boundary, the VIMF easterly outflow is stronger over the tropics than in ERA5 (Fig. 13e, f) and over the subtropics (Figs. 13e-13f and A3k), although a somewhat weaker outflow is found in the ensemble mean at the low-levels over the tropics (Supplementary Fig. A3k). Over the eastern boundary, the ensemble mean easterly inflow of vapor flux is stronger than in ERA5 over the tropics and parts of the subtropics, while the outflow of westerly vapor flux is slightly stronger over the extratropics (Fig. 13g, h and Supplementary Fig. A3l). These boundary conditions are relevant for the interpretation and/or model calibration when using limited area models (e.g. Regional Climate Models (RCMs)) for dynamical downscaling of CMIP6 models.

4.2 Vertically integrated energy fluxes

Figure 14 shows the VIHF transects over the South American boundaries for the DJF and JJA seasons. The northern VIHF has a marked northerly peak centered about 50º W during DJF but acquires a generally uniform pattern during JJA (Figs. 14a-14b). The southern VIHF shows northerly fluxes over the 95º W-65º W longitudinal range and southerly fluxes in the 65º–35º W zonal band (Figs. 14c-14d). Both zonal fluxes through the western and eastern boundaries show westerly fluxes in the extratropical latitudes and more easterly fluxes over the tropics (Fig. 14e, h). The CMIP6 models follow the pattern suggested by the ERA5 dataset for the VIHF across all the boundaries, suggesting that the models are able to capture these boundary heat fluxes in South America. The multimodel ensemble captures the VIHF transect across the four boundaries considered. Similar to the moisture fluxes, the models show a much better representation of the DJF zonal heat fluxes, which are higher in magnitude than the meridional fluxes (Supplementary Fig. A4e–h), as also observed for the moisture fluxes (Supplementary Fig. A3e–h).

5 Performance evaluation and model ranking

The main objective of this work is to provide a ranking of CMIP6 models according to their performance in the simulation of circulation features and spatial fields as well as moisture and heat fluxes across the continental boundaries for South America. Our evaluation aims to provide useful input for the selection of climate models to force regional simulations in South America. Supplementary Figures A5 and A6 show the model ranking for each of the regional circulation features evaluated from index estimates (ATW, SPW, BH, SHSJ, SHPJ, ENSO power spectrum, and subtropical highs), based on the Ranking Score (*RS*). Similarly, Figure A7 shows the model ranking for the vertically integrated moisture and heat fluxes across the South American boundaries for the austral summer (DJF) and winter (JJA). A *RS* close to 1 (red colors) indicates that the model is among the best models simulating a particular feature, according to the correlation coefficient (Supplementary Figs. A5a, A6a, and A7a) or the RMSE (Supplementary Figs. A5b, A6b and A7b). In addition, Tables A2-A10 show the best 5 CMIP6 models for each feature. These results show that no single model is among the best models in representing all the features considered in this evaluation, with the model

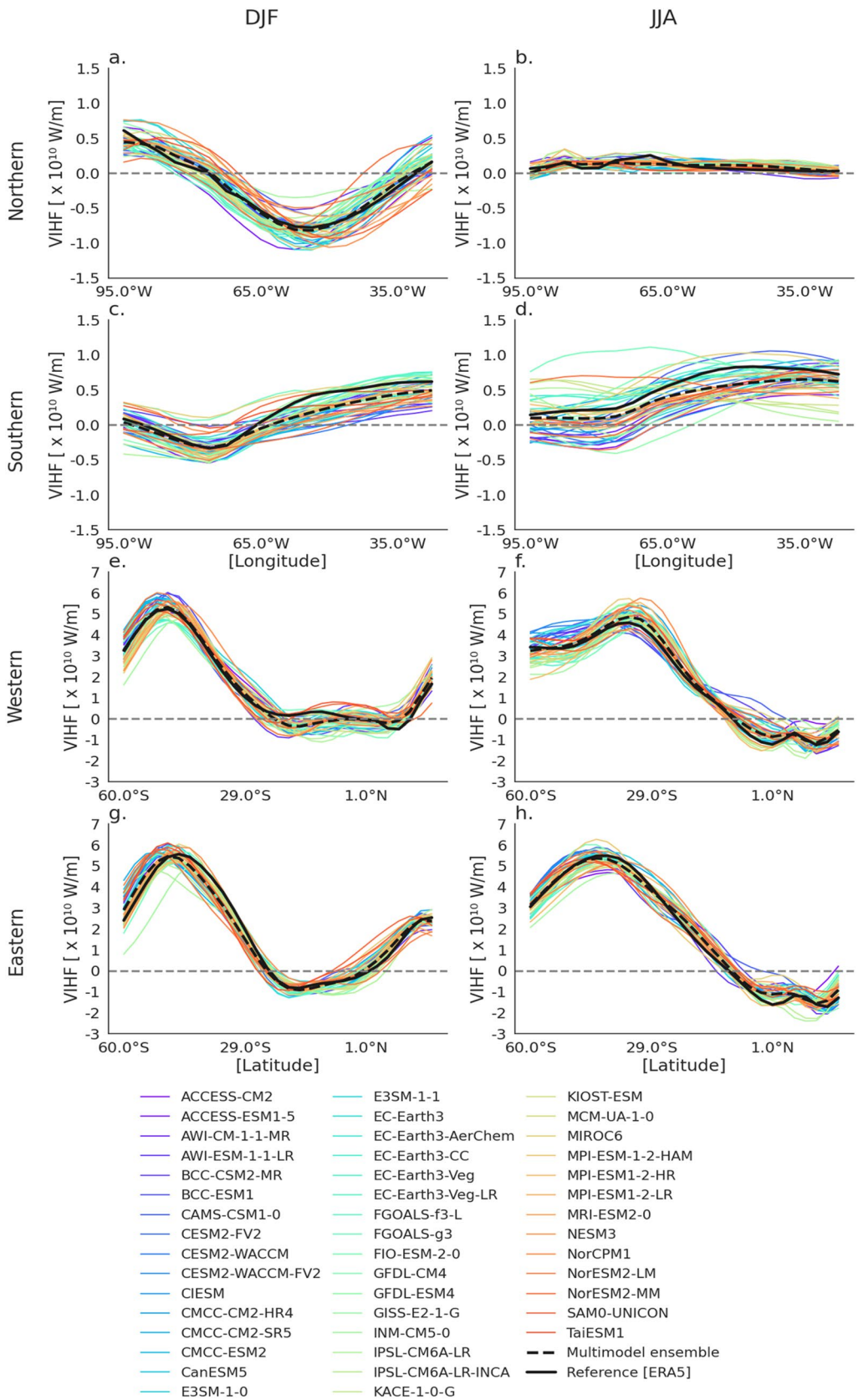
DJF
JJA
a.
b.
c.
d.
e.
f.
g.
h.
Northern
Southern
Western
Eastern
VIHF [x 10¹⁰ W/m]
95.0°W
65.0°W
35.0°W
[Longitude]
60.0°S
29.0°S
1.0°N
[Latitude]
ACCESS-CM2
ACCESS-ESM1-5
AWI-CM-1-1-MR
AWI-ESM-1-1-LR
BCC-CSM2-MR
BCC-ESM1
CAMS-CSM1-0
CESM2-FV2
CESM2-WACCM
CESM2-WACCM-FV2
CIESM
CMCC-CM2-HR4
CMCC-CM2-SR5
CMCC-ESM2
CanESM5
E3SM-1-0
E3SM-1-1
EC-Earth3
EC-Earth3-AerChem
EC-Earth3-CC
EC-Earth3-Veg
EC-Earth3-Veg-LR
FGOALS-f3-L
FGOALS-g3
FIO-ESM-2-0
GFDL-CM4
GFDL-ESM4
GISS-E2-1-G
INM-CM5-0
IPSL-CM6A-LR
IPSL-CM6A-LR-INCA
KACE-1-0-G
KIOST-ESM
MCM-UA-1-0
MIROC6
MPI-ESM-1-2-HAM
MPI-ESM1-2-HR
MPI-ESM1-2-LR
MRI-ESM2-0
NESM3
NorCPM1
NorESM2-LM
NorESM2-MM
SAM0-UNICON
TaiESM1
Multimodel ensemble
Reference [ERA5]

◂**Fig. 14** Climatological Vertically Integrated Heat Flux (VIHF) estimated from the dry static energy (DSE; Eqs. 3 and 4) across the a)-b) northern, c)-d) southern, e)-f) western, and g)-h) eastern boundaries of the South American domain (see Fig. 1b) for December-February (DJF) and June–August (JJA) for the different CMIP6 models available and the reference ERA5 dataset (thick black line). For comparison, the multimodel ensemble is shown (thick dotted black line)

performance depending on the metric used (correlation coefficient or RMSE).

Supplementary Tables A11–A20 show the Taylor Skill Score (*TS*) for the seasonal spatial patterns of 850 hPa winds, 200 hPa winds, SLP, SST, DJF El Niño SSTAs, precipitation, regional Walker cell, regional Hadley cell, as well as the DJF vertical structure of the moisture and heat fluxes across the boundaries in the South American domain, based on the Taylor diagrams (Figs. 2, 5, 8, 9, 10, 11 and 12 and Supplementary Fig. A2–A4). Although these spatial patterns are not representative of specific circulation features, they are commonly considered when performing model evaluation. As also indicated by the Taylor diagrams, the models better simulate the seasonal patterns of SST/SLP (*TS* above 0.9), 850 hPa/200 hPa winds (*TS* around 0.7–0.9), and the vertical structure of the moisture/heat fluxes across the South American boundaries (*TS* around 0.7–0.9). By contrast, the models have a poor performance reproducing DJF El Niño SSTA (0.1–0.4) and the seasonal patterns of precipitation (0.3–0.6) (Tables A11-A20).

Regarding seasonal performance, models have higher *TS* for 850 hPa wind in SON (austral spring), 250 hPa wind/precipitation in JJA (austral winter) and SON, the Walker/Hadley cells in DJF (austral summer), and SLP/SST for all seasons. The vertical structure of the moisture and heat fluxes across the domain boundaries are better represented for the eastern and western boundaries (zonal fluxes), as also suggested by the VIMF/VIHF transects (Fig. 13 and 14).

The *TS* indicates that, in many cases, the best 5 models representing the spatial pattern of a particular variable do it for more than one season. However, no single model exhibits the best performance in the simulation of all these spatial patterns (Supplementary Tables A11–A20), highly depending on the variable considered, as also observed for the circulation features evaluated from indices (Supplementary Tables A2–A10).

Given the large diversity of model performance for the different features and spatial patterns considered, our results highlight the importance of conducting a process-based model evaluation when selecting the GCMs or ESMs to force regional models. In the case of CMIP6 models and South America, the rankings provided in Tables A2-A10 can be useful to guide the selection of model output for dynamical downscaling. For example, for RCM simulations with a focus over northern South America, the features listed in Table 1 could be among the most relevant. The corresponding rankings suggest that output from the family of GFDL models could be useful for dynamical downscaling, since it has a good representation of the seasonal behavior of the NASH and ENSO related frequencies. Another good candidate could come from the family of MPI-ESM models, which have a good representation of the trade winds, the easterly VIMF and the latitude of the NASH. In contrast, for a domain focused on southwestern South America, the relevant features could be like those listed in Table 2. In this case, the best compromise could be offered by output from FGOALS-f3-L, with a good representation of westerly winds, westerly VIMF, the SHSJ and the SPSH. The CESM2 model family also looks as a good source, followed by the family of MPI-ESM. Note that the GFDL model family does not stand out for the features in Table 2.

6 Summary and conclusions

This work addresses an evaluation of a large set of CMIP6 models (57 models available at https://esgf-node.llnl.gov/search/cmip6) in simulating key spatial patterns and circulation features over South America. Our findings provide valuable guidance for selecting outputs from specific GCMs and ESMs as boundary conditions for regional simulations in the South American domain.

Although many previous studies have focused on the evaluation of climate models in their simulation of the spatial patterns of different variables over South America (mainly air surface temperature and precipitation at annual and seasonal scales) (e.g. Yin et al. 2013; Gonzalez et al. 2014; Gulizia and Camiloni 2015; Palomino-Lemus et al. 2015, 2017; Sierra et al. 2015; Tedeschi and Collins 2015; Bonilla-Ovalle and Mesa-Sánchez 2017; Zazulie et al. 2018; Rivera and Arnould 2020; Vasconcellos et al. 2020; Almazroui et al. 2021; Arias et al. 2021b; Díaz et al. 2021; Ortega et al. 2021; Vale et al. 2021; Varuolo-Clarke et al. 2021; Firpo et al. 2022; Vicente-Serrano et al. 2022; Marianetti et al. 2024), fewer studies have focused on specific circulation features (Barros and Doyle 2018; Sierra et al. 2018, 2021; Flores-Aqueveque et al. 2020; Olmo et al. 2022b; Valencia and Mejía 2022; Agudelo et al. 2023; Arias et al. 2023; Bazzanela et al. 2024; Correa et al. 2024) and even fewer have addressed boundary conditions relevant for regional simulations.

Recent work by Zhang et al. (2024) assessed 37 CMIP6 models in simulating large-scale driving fields over the South American domain for the Coordinated Regional Climate Downscaling Experiment (CORDEX). This work is an important step for a systematic evaluation of CMIP6 models in South America. As a further contribution to achieve a robust evaluation of CMIP6 models, our study

focuses on specific circulation features relevant to South America's climate and addresses how models represent moisture and heat fluxes across the continent's boundaries—critical elements for regional simulations forced by global climate models.

Our study expands on this by evaluating CMIP6 models in terms of their simulation of key circulation patterns, such as the Atlantic Trade Winds, the Pacific Westerlies, the Bolivian High (BH), the Subtropical Jet, the Polar jet, and the regional Walker and Hadley cells. We also analyzed the models' ability to reproduce ENSO-related SST anomalies and the associated Niño3 index spectrum, as well as moisture and heat fluxes across South American boundaries, which are crucial for regional downscaling.

We used the Taylor Skill Score (*TS*) to rank the models according to their simulation of the spatial patterns considered (Figs. 2, 5, 8, 9, 10, 11, 12, 13, 14 and Supplementary A2–A4). For the features evaluated from index estimates (Figs. 3, 4, 6, 7, 13, 14 and Supplementary A1–A2), we used the correlation coefficient and the root mean square error (RMSE). Figures A5-A7 and Tables A2-A20 summarize the ranking obtained from our analysis. In Supplementary Figs. A5-A7, a Ranking Score (*RS*) close to 1 (red colors) indicates a better model performance while a *RS* close to 0 (blue colors) correspond to a poor performance. Tables A2-A20 list the best 5 models in the simulation of each feature/spatial pattern considered.

The CMIP6 models show higher skills at simulating the seasonal patterns of SLP/SST (Tables A15–A16), with medium skills simulating 850 hPa/200 hPa winds (Tables A11-A12) and the vertical structure of the moisture/heat fluxes across the South American boundaries (Tables A19-A20). In particular, the vertical structure of the moisture and heat fluxes across the domain boundaries is better represented for the eastern and western boundaries (zonal fluxes) (Figs. 13, 14 and Supplementary Tables A19–A20). The poorest performance is observed for the seasonal patterns of precipitation (Table A18) and the El Niño SSTAs (Table A17). This poor ENSO simulation is also identified in the Fourier spectrum of the Niño3.4 index, since a first

Table 1 Top 5 models according to their performance for some of the evaluated features (based on correlation), including examples that could be more relevant for northern South America

Ranking	Trade Winds	ENSO Spectrum	NASH latitude	NASH longitude	NASH strength	VIMF North JJA	VIMF East JJA
1	SAM0-UNICON	EC-Earth3-CC	IPSL-CM6A-LR	GFDL-CM4	GISS-E2-1-G	EC-Earth3-Veg-LR	CMCC-CM2-HR4
2	GISS-E2-1-G	CIESM	CAS-ESM2-0	GISS-E2-2-H	GFDL-CM4	EC-Earth3-Veg	E3SM-1–0
3	FGOALS-g3	GFDL-ESM4	MPI-ESM-1–2-HAM	IPSL-CM6A-LR	BCC-CSM2-MR	EC-Earth3-CC	CMCC-ESM2
4	E3SM-1–1	INM-CM4-8	EC-Earth3-Veg-LR	EC-Earth3	GISS-E2-2-H	GFDL-ESM4	MPI-ESM1-2-HR
5	MPI-ESM-1–2-HAM	FIO-ESM-2–0	GFDL-CM4	GISS-E2-1-G	INM-CM5-0	EC-Earth3-AerChem	CanESM5

See Supplementary Tables A2–A8

Table 2 Top 5 models according to their performance for some of the evaluated features (based on correlation), including examples that could be more relevant for southwestern South America

Ranking	Westerlies strength	SHSJ latitude	SPSH latitude	SPSH longitude	SPSH strength	VIMF South JJA	VIMF West JJA
1	FGOALS-f3-L	SAM0-UNICON	CESM2-WACCM	BCC-CSM2-MR	NorCPM1	EC-Earth3-CC	MPI-ESM1-2-LR
2	ACCESS-CM2	CESM2	E3SM-1–0	CESM2-WACCM	FIO-ESM-2–0	CESM2-WACCM	FGOALS-f3-L
3	IPSL-CM5A2-INCA	FGOALS-f3-L	NorESM2-MM	MPI-ESM1-2-HR	EC-Earth3-Veg	NorCPM1	MRI-ESM2-0
4	MPI-ESM-1–2-HAM	GISS-E2-1-H	E3SM-1–1-ECA	SAM0-UNICON	GISS-E2-2-H	CIESM	EC-Earth3-Veg-LR
5	CanESM5	CMCC-CM2-SR5	SAM0-UNICON	INM-CM4-8	FGOALS-f3-L	MPI-ESM1-2-LR	EC-Earth3-AerChem

See Supplementary Tables A2–A8

group of models underestimate the dominant ENSO frequency (4–5 years) with frequencies about 2–3 years while a second set of models show longer frequencies of more than 5 years (Supplementary Fig. A2c).

This shows that although the models show a very good skill simulating the seasonal SST patterns (Table A16), they show strong biases simulating the ENSO-related SSTAs and their frequencies (Table A17 and Supplementary Fig. A2), suggesting challenges in the simulation of interannual variability in eastern Pacific SSTs. The CMIP6 biases in ENSO simulations have been widely reported in the literature. For instance, CMIP6 models exhibit challenges to adequately simulate the ENSO peak activity during boreal winter (a.k.a ENSO seasonal phase-locking), associated with difficulties in their simulation of the seasonal cycle of the zonal SST gradient in the equatorial Pacific during boreal spring and autumn (Liao et al. 2021), affecting the zonal wind-SST feedback (Beobide-Arsuaga et al. 2021). In particular, the simulation of the cold tongue strength over the equatorial western Pacific largely modulates the ENSO SST biases in these models (Jiang et al. 2021). In addition, CMIP6 models underestimate ENSO teleconnections in the Southern Hemisphere due to underestimations in wave trains from the tropical Pacific to the Amundsen Sea (Fang et al. 2024), which is particularly relevant for South America.

The CMIP6 models exhibit a very good resemblance of the seasonal SLP patterns (Table A15) but their performance in the representation of the subtropical highs over the surrounding oceans of South America is much poorer, particularly for the longitudinal location of these anticyclones (Supplementary Fig. A1). In addition, the CMIP6 models better simulate the annual cycle of the Westerlies strength (Fig. 4a) than that for the Westerlies latitudinal location (Fig. 4b) and the Trade Winds index (Fig. 3). In general, the models better resemble the upper-level circulation associated with the BH, as well as the Subtropical and Polar Jets, than the lower-level circulation, in terms of the annual cycle of these features (compare Figs. 3, 4 with Figs. 6, 7). Bazzanela et al. (2024) highlight the satisfactory performance of the CMIP6 models in their simulation of the BH position.

Note that some models represent a too strong influx of moisture through the northern boundary (Fig. 13a, b), which would be available for moist processes within an RCM simulation for South America. Other models are on the other side of the spectrum. In the case of the zonal VIMF, some models represent a too strong easterly flow on the western boundary over tropical latitudes (Fig. 13f), which might represent a boundary condition that could weaken some patterns of convergence over the eastern Pacific, relevant for tropical South America. A similar situation could happen over the southeastern boundary (Fig. 13g), regarding westerly flow and convergence over the southern Atlantic. This information is relevant for the interpretation and/or model configuration for downscaling with limited area models (including RCMs).

In conclusion, our study provides clear evidence that CMIP6 models perform better in simulating large-scale circulation patterns than in capturing regional precipitation and SST variability. Furthermore, no single model excels across all the evaluated features, underscoring the need for a process-based model evaluation when selecting GCMs or ESMs for regional simulations in South America. To our knowledge, this is the first comprehensive evaluation of CMIP6 models that considers such a broad range of climate features over the entire South American continent.

While this study does not delve into the causes of model biases, the rankings provided here offer a valuable foundation for further research aimed at understanding these biases in detail. Therefore we encourage further studies to analyze climatic processes related to the biases in the specific spatial patterns and circulation features identified in this work. The evaluation provided in this study serves as a first step toward selecting optimal CMIP6 models for regional climate simulations, which are critical for assessing the impacts of climate change on a highly vulnerable continent like South America (Castellanos et al. 2022) that faces significant adaptation challenges (Cavazos et al. 2024).

Supplementary Information The online version contains supplementary material available at https://doi.org/10.1007/s00382-025-07704-w.

Acknowledgements This work was developed within the ANDEX Hydroclimatology Program as a contribution of the Disciplinary Team on Environmental and Ecological Changes and the Transversal Line on Numerical Modeling (https://www.andex-rhp.org/). To process the data, this study benefited from the IPSL Data and Computing ESPRI, supported by CNRS, SU, CNES and Ecole Polytechnique.

Author contributions All authors designed the research. I.C.C. wrote the scripts, processed data, and prepared all figures. L.F prepared and ran the scripts. P.A.A analyzed the results and wrote the manuscript. All authors reviewed the manuscript and contributed to the analyses and discussion.

Funding Open Access funding provided by Colombia Consortium. This work was funded by CLIMAT-AmSud through the grant 21-CLIMAT-01 (Interaction between large-scale Atmospheric Circulation and dEforestation in the southern Amazon: implications for the local and continental water cycle—ACE-Amazon) and CLIMAT-AmSud HighRes-AmSur grant 22-CLIMAT-05. Regional funding was provided through MINCIENCIAS grant 80740–238-2021 (Colombia), ANID grant CLI2020002 (Chile), and FONDECYT grant 190–2020 (Peru). In addition, Paola A. Arias, Isabel C. Correa and J. Alejandro Martinez were funded by MINCIENCIAS through program No. 80740–490-2020 and Universidad de Antioquia through grant TEM2022-55390. Juan P. Boisier and Camila Alvarez-Garreton were funded by FONDAP/ANID 1523A0002 (Chile).

Availability of data and materials ERA5 data is available at the ECMWF portal: https://www.ecmwf.int/en/forecasts/datasets/reana

lysis-datasets/era5. CMIP6 data is available at the ESGF portal: https://esgf-node.llnl.gov/projects/cmip6/.

Declarations

Conflicts of interest The authors declare no conflicts of interest or competing interests.

Ethical approval Not applicable.

References

Agudelo J, Espinoza JC, Junquas C, Arias PA, Sierra JP, Olmo ME (2023) Future projections of low-level atmospheric circulation patterns over South Tropical South America: Impacts on precipitation and Amazon dry season length. J Geophys Res 128:e2023JD038658. https://doi.org/10.1029/2023JD038658

Almazroui M, Ashfaq M, Islam MN et al (2021) Assessment of CMIP6 Performance and Projected Temperature and Precipitation Changes Over South America. Earth Syst Environ 5:155–183. https://doi.org/10.1007/s41748-021-00233-6

Amador JA (2008) The Intra-Americas Sea Low-level Jet. Ann NY Acad Sci 1146:153–188. https://doi.org/10.1196/annals.1446.012

Arias PA, Martínez JA, Vieira SC (2015) Moisture sources to the 2010–2012 anomalous wet season in northern South America. Clim Dyn 45:2861–2884. https://doi.org/10.1007/s00382-015-2511-7

Arias PA, Martínez JA, Mejía JD, Pazos MJ, Espinoza JC (2020) Changes in normalized difference vegetation index in the Orinoco and Amazon river basins: links to tropical atlantic surface temperatures. J Clim 33(19):8537–8559. https://doi.org/10.1175/jcli-d-19-0696.1

Arias PA, Garreaud R, Poveda G, Espinoza JC, Molina-Carpio J et al (2021a) Hydroclimate of the Andes. Part II: Hydroclimate variability and sub-continental patterns. Fron Earth Sci 8:1–25. https://doi.org/10.3389/feart.2020.505467

Arias PA, Ortega G, Villegas LD, Martínez JA (2021b) Colombian climatology in CMIP5/CMIP6 models: Persistent biases and improvements. Revista Facultad De Ingeniería Universidad De Antioquia 100:75–96. https://doi.org/10.17533/udea.redin.20210525

Arias PA, Rendón ML, Martínez JA, Allan RP (2023) Changes in atmospheric moisture transport over tropical South America: an analysis under a climate change scenario. Clim Dyn 61:4949–4969. https://doi.org/10.1007/s00382-023-06833-4

Baker JCA, Spracklen DV (2022) Divergent representation of precipitation recycling in the Amazon and the Congo in CMIP6 models. Geophyis Res Lett 49:e2021GL095136. https://doi.org/10.1029/2021GL095136

Baker JCA, Garcia-Carreras L, Buermann B et al (2021) Robust Amazon precipitation projections in climate models that capture realistic land–atmosphere interactions. Environ Res Lett 16:074002. https://doi.org/10.1088/1748-9326/abfb2e

Barichivich J, Gloor E, Peylin P, Brienen RJW, Schönegart J, Espinoza JC, Pattnayak KC (2018) Recent intensification of Amazon flooding extremes driven by strengthened Walker circulation. Sci Adv. https://doi.org/10.1126/sciadv.aat8785

Barros VR, Doyle ME (2018) Low-level circulation and precipitation simulated by CMIP5 GCMS over southeastern South America. Int J Climatol 38:5476–5490. https://doi.org/10.1002/joc.5740

Bazzanela AC, Dereczynski C, Luiz-Silva W et al (2024) Performance of CMIP6 models over South America. Clim Dyn 62:1501–1516. https://doi.org/10.1007/s00382-023-06979-1

Beobide-Arsuaga G, Bayr T, Reintges A et al (2021) Uncertainty of ENSO-amplitude projections in CMIP5 and CMIP6 models. Clim Dyn 56:3875–3888. https://doi.org/10.1007/s00382-021-05673-4

Boisier JP, Rondanelli R, Garreaud RD, Muñoz F (2016) Anthropogenic and natural contributions to the Southeast Pacific precipitation decline and recent megadrought in central Chile. Geophys Res Lett 43:413–421. https://doi.org/10.1002/2015GL067265

Bonilla-Ovallos CA, Mesa-Sánchez OJ (2017) Validación de la precipitación estimada por modelos climáticos acoplados del proyecto de intercomparación CMIP5 en Colombia. Revista De La Academia Colombiana De Ciencias Exactas, Físicas y Naturales 41(158):107–118. https://doi.org/10.18257/raccefyn.427

Brands S, Herrera S, Fernández J et al (2013) How well do CMIP5 Earth System Models simulate present climate conditions in Europe and Africa? Clim Dyn 41:803–817. https://doi.org/10.1007/s00382-013-1742-8

Cai W, McPhaden M, Grimm A, Rodrigues R, Taschetto A, Garreaud R et al (2020) Climate impacts of El Niño-Southern Oscillation on South America. Nat Rev Earth Environ 1:215–231. https://doi.org/10.1038/s43017-020-0040-3

Campozano L, Trachte K, Célleri R, Samaniego E, Bendix J, Albuja C et al (2018) Climatology and teleconnections of mesoscale convective systems in an Andean basin in southern Ecuador: the case of the Paute basin. Adv Meteorol 2018:1–13. https://doi.org/10.1155/2018/4259191

Campozano L, Robaina L, Samaniego E (2020) The Pacific Decadal Oscillation modulates the relation of ENSO with the rainfall variability in coast of Ecuador. Int J Climatol 40(13):5801–5812. https://doi.org/10.1002/joc.6525

Castellanos E, Lemos MF, Astigarraga L, Chacón N, Cuvi N et al (2022) Central and South America. In: Pörtner H-O, Roberts DC, Tignor M, Poloczanska ES, Mintenbeck K, Alegría A, Craig M, Langsdorf S, Löschke S, Möller V, Okem A, Rama B (eds) Climate change 2022: impacts, adaptation and vulnerability. Contribution of Working Group II to the Sixth Assessment Report of the Intergovernmental Panel on Climate Change. Cambridge University Press, Cambridge, pp 1689–1816. https://doi.org/10.1017/9781009325844.014

Cavazos T, Bettolli ML, Campbell D et al (2024) Challenges for climate change adaptation in Latin America and the Caribbean region. Front Clim 6:1392033. https://doi.org/10.3389/fclim.2024.1392033

Chavez SP, Takahashi K (2017) Orographic rainfall hotspots in the Andes-Amazon transition according to the TRMM precipitation radar and in situ data. J Geophys Res 122:5870–5882. https://doi.org/10.1002/2016JD026282

Collazo S, Barrucand M, Rusticucci M (2022) Evaluation of CMIP6 models in the representation of observed extreme temperature indices trends in South America. Clim Change 172:21. https://doi.org/10.1007/s10584-022-03376-1

Correa IC, Arias PA, Vieira SC, Martinez JA (2024) A drier Orinoco basin during the 21st century: the role of the Orinoco

low-level jet. Clim Dyn 62:2369–2398. https://doi.org/10.1007/s00382-023-07028-7
de Medeiros FJ, de Oliveira CP, Avila-Diaz A (2022) Evaluation of extreme precipitation climate indices and their projected changes for Brazil: From CMIP3 to CMIP6. Weather Clim Extremes 38:100511. https://doi.org/10.1016/j.wace.2022.100511
Dias CG, Reboita MS (2021) Assessment of CMIP6 Simulations over Tropical South America. Revista Brasileira De Geografia Física. https://doi.org/10.26848/rbgf.v14.3.p1282-1295
Díaz LB, Vera CS (2018) South American precipitation changes simulated by PMIP3/CMIP5 models during the Little Ice Age and the recent global warming period. Int J Climatol 38:2638–2650. https://doi.org/10.1002/joc.5449
Díaz LB, Saurral RI, Vera CS (2021) Assessment of South America summer rainfall climatology and trends in a set of global climate models large ensembles. Int J Climatol 41(Suppl. 1):E59–E77. https://doi.org/10.1002/joc.6643
Doyle ME, Barros VR (2002) Midsummer low-level circulation and precipitation in subtropical South America and Related Sea Surface Temperature Anomalies in the South Atlantic. J Clim 15:3394–3410. https://doi.org/10.1175/1520-0442(2002)015%3c3394:MLLCAP%3e2.0.CO;2
Drumond A, Nieto R, Gimeno L, Ambrizzi T (2008) A Lagrangian identification of major sources of moisture over Central Brazil and La Plata Basin. J Geophys Res 113:D14128. https://doi.org/10.1029/2007JD009547
Drumond A, Nieto R, Trigo R, Ambrizzi T, Souza E, Gimeno L (2010) A Lagrangian Identification of the Main Sources of Moisture Affecting Northeastern Brazil during Its Pre-Rainy and Rainy Seasons. PLoS ONE 5(6):e11205. https://doi.org/10.1371/journal.pone.0011205
Escobar M, Hoyos I, Nieto R, Villegas JC (2022) The importance of continental evaporation for precipitation in Colombia: a baseline combining observations from stable isotopes and modelling moisture trajectories. Hydrol Processes 36(6):e14595. https://doi.org/10.1002/hyp.14595
Espinoza JC, Chavez S, Ronchail J, Junquas C, Takahashi K, Lavado W (2015) Rainfall hotspots over the southern tropical Andes: spatial distribution, rainfall intensity and relations with large scale atmospheric circulation. Water Resour Res 51:3459–3475. https://doi.org/10.1002/2014wr016273
Espinoza JC, Ronchail J, Marengo JA, Segura H (2019) Contrasting North-South changes in Amazon wet-day and dry-day frequency and related atmospheric features (1981–2017). Clim Dyn 52:5413–5430. https://doi.org/10.1007/s00382-018-4462-2
Espinoza JC, Garreaud R, Poveda G, Arias PA, Molina-Carpio J et al (2020) Hydroclimate of the Andes. Part I: main climatic features. Front Earth Sci 8:64. https://doi.org/10.3389/feart.2020.00064
Espinoza JC, Marengo JA, Schongart J, Jimenez JC (2022) The new historical flood of 2021 in the Amazon River compared to major floods of the 21st century: Atmospheric features in the context of the intensification of floods. Weather Clim Extremes 35:100406. https://doi.org/10.1016/j.wace.2021.100406
Eyring V, Bony S, Meehl GA, Senior CA, Stevens B, Stouffer RJ, Taylor KE (2016) Overview of the Coupled Model Intercomparison Project Phase 6 (CMIP6) experimental design and organization. Geosci Model Dev 9:1937–1958. https://doi.org/10.5194/gmd-9-1937-2016
Fang Y, Screen JA, Hu X et al (2024) CMIP6 models underestimate ENSO teleconnections in the Southern Hemisphere. Geophys Res Lett 51:e2024GL110738. https://doi.org/10.1029/2024GL110738
Firpo MÂF, Guimarães BDS, Dantas LG et al (2022) Assessment of CMIP6 models' performance in simulating present-day climate in Brazil. Front Clim 4:948499. https://doi.org/10.3389/fclim.2022.948499
Flores-Aqueveque V, Rojas M, Aguirre C, Arias PA, González C (2020) South Pacific Subtropical High from the late Holocene to the end of the 21st century: insights from climate proxies and general circulation models. Clim past 16(1):79–99. https://doi.org/10.5194/cp-16-79-2020
Garreaud RD (2009) The Andes climate and weather. Adv Geosci 22:3–11. https://doi.org/10.5194/adgeo-22-3-2009
Garreaud RD (2018) A plausible atmospheric trigger for the 2017 coastal El Niño. Int J Climatol 38:1296–1302. https://doi.org/10.1002/joc.5426
Garreaud R, Muñoz R (2005) The low-level jet off the subtropical west coast of South America: structure and variability. Mon Weather Rev 133:2246–2261. https://doi.org/10.1175/mwr2972.1
Garreaud RD, Vuille M, Compagnucci R, Marengo J (2009) Present-day South American climate. Palaeogeogr Palaeoclimatol Palaeoecol 281:180–195. https://doi.org/10.1016/j.palaeo.2007.10.032
Garreaud RD, Boisier JP, Rondanelli R, Montecinos A, Sepúlveda HH, Veloso-Aguila D (2020) The central Chile mega drought (2010–2018): a climate dynamics perspective. Int J Climatol 40:421–439. https://doi.org/10.1002/joc.6219
Gillett NP, Kell TD, Jones PD (2006) Regional climate impacts of the southern annular mode. Geophys Res Lett 33(23). https://doi.org/10.1029/2006GL027721
Gimeno L, Stohl A, Trigo RM, Dominguez F, Yoshimura K, Yu L, Drumond A, Durán-Quesada AM, Nieto R (2012) Oceanic and terrestrial sources of continental precipitation. Rev Geophys 50:RG4003. https://doi.org/10.1029/2012RG000389
Gimeno L, Dominguez F, Nieto R, Trigo R, Drumond A et al (2016) Major mechanisms of atmospheric moisture transport and their role in extreme precipitation events. Annu Rev Environ Resour 41(1):117–141. https://doi.org/10.1146/annurev-environ-110615-085558
Gonzalez PLM, Polvani LM, Seager R et al (2014) Stratospheric ozone depletion: a key driver of recent precipitation trends in South Eastern South America. Clim Dyn 42:1775–1792. https://doi.org/10.1007/s00382-013-1777-x
Gulizia C, Camilloni I (2015) Comparative analysis of the ability of a set of CMIP3 and CMIP5 global climate models to represent precipitation in South America. Int J Climatol 35:583–595. https://doi.org/10.1002/joc.4005
Gulizia CN, Raggio GA, Camilloni IA et al (2022) Changes in mean and extreme climate in southern South America under global warming of 1.5 °C, 2 °C, and 3 °C. Theor Appl Climatol 150:787–803. https://doi.org/10.1007/s00704-022-04199-x
Hersbach H, Bell B, Berrisford P et al (2020) The ERA5 global reanalysis. Q J R Meteorol Soc 146:1999–2049. https://doi.org/10.1002/qj.3803
Hirota N, Takayabu YN (2013) Reproducibility of precipitation distribution over the tropical oceans in CMIP5 multi-climate models compared to CMIP3. Clim Dyn 41:2909–2920. https://doi.org/10.1007/s00382-013-1839-0
Hoorn C, Wesseling P, ter Steege H, Bermudez MA, Mora A, Sevink J et al (2010) Amazonia through time: Andean uplift, climate change, landscape evolution, and biodiversity. Science 330:927–931. https://doi.org/10.1126/science.11
Hoyos IC, Dominguez F, Cañón-Barriga JE, Martínez JA, Nieto R, Gimeno L et al (2018) Moisture origin and transport processes in Colombia, northern South America. Clim Dyn 50:971–990. https://doi.org/10.1007/s00382-017-3653-6
Imfeld N, Sedlmeier K, Gubler S, Marrou KC, Davila CP, Huerta A et al (2020) A combined view on precipitation and temperature climatology and trends in the southern Andes of Peru. Int J Climatol. https://doi.org/10.1002/joc.6645

Jacques-Coper M, Garreaud RD (2015) Characterization of the 1970s climate shift in South America. Int J Climatol 35:2164–2179. https://doi.org/10.1002/joc.4120

Jiang W, Huang P, Huang G, Ying J (2021) Origins of the excessive westward extension of ENSO SST simulated in CMIP5 and CMIP6 models. J Clim 34:2839–2851. https://doi.org/10.1175/JCLI-D-20-0551.1

Jiménez-Sánchez G, Markowski PM, Jewtoukoff V, Young GS, Stensrud DJ (2019) The Orinoco low-level jet: an investigation of its characteristics and evolution using the WRF model. J Geophys Res Atmos 124:10696–10711. https://doi.org/10.1029/2019JD030934

Jones C, Carvalho LMV (2013) Climate Change in the South American Monsoon System: Present Climate and CMIP5 Projections. J Clim 26(17):6660–6678. https://doi.org/10.1175/JCLI-D-12-00412.1

Jones C, Carvalho LMV (2018) The influence of the Atlantic Multidecadal Oscillation on the eastern Andes low-level jet and precipitation in South America. NPJ Clim Atmos Sci 1:1–7. https://doi.org/10.1038/s41612-018-0050-8

Junquas C, Vera CS, Li L, Le Treut H (2012) Summer precipitation variability over Southeastern South America in a global warming scenario. Clim Dyn 38(9):1867–1883. https://doi.org/10.1007/s00382-011-1141-y

Junquas C, Takahashi K, Condom T, Espinoza JC, Chavez S, Sicart JE et al (2018) Understanding the influence of orography over the precipitation diurnal cycle and the associated atmospheric processes in the central Andes. Clim Dyn 50:3995–4017. https://doi.org/10.1007/s00382-017-3858-8

Kayano MT, Capistrano VB (2014) How the Atlantic Multidecadal Oscillation (AMO) modifies the ENSO influence on the South American rainfall. Int J Climatol 34:162–178. https://doi.org/10.1002/joc.3674

Kayano MT, Andreoli RV, Souzade RAF (2019) El Niño-Southern Oscillation related teleconnections over South America under distinct Atlantic Multidecadal Oscillation and Pacific Interdecadal Oscillation backgrounds: La Niña. Int J Climatol 39:1359–1372. https://doi.org/10.1002/joc.5886

Kayano MT, Cerón WL, Andreoli RV, Souza RAF, Avila-Diaz A, Zuluaga CF, Carvalho LMV (2022) Does the El Niño-Southern Oscillation affect the combined impact of the Atlantic Multidecadal Oscillation and Pacific Decadal Oscillation on the Precipitation and Surface Air Temperature Variability over South America? Atmos 13(2):231. https://doi.org/10.3390/atmos13020231

Lenters JD, Cook KH (1997) On the origin of the Bolivian high and related circulation features of the South American climate. J Atmos Sci 54:656–677. https://doi.org/10.1175/1520-0469(1997)054%3c0656:OTOOTB%3e2.0.CO;2

Leyba IM, Solman SA, Saraceno M et al (2023) The South Atlantic Ocean as a moisture source region and its relation with precipitation in South America. Clim Dyn 61:1741–1756. https://doi.org/10.1007/s00382-022-06653-y

Liao H, Chunzai W, Zhenya S (2021) ENSO phase-locking biases from the CMIP5 to CMIP6 models and a possible explanation. Deep Sea Res Part II 189–190:104943. https://doi.org/10.1016/j.dsr2.2021.104943

Loaiza-Cerón W, Andreoli RV, Kayano MT, Ferreira de Souza RA, Jones C, Carvalho LMV (2020) The influence of the Atlantic Multidecadal Oscillation on the Choco low-level jet and precipitation in Colombia. Atmosphere 11:174. https://doi.org/10.3390/atmos11020174

Londoño-Arteaga V, Lima CHR (2021) Analysis of CMIP 5 simulations of key climate indices associated with the South America monsoon system. Int J Climatol 41:404–422. https://doi.org/10.1002/joc.6627

Marengo JA, Soares WR, Saulo C, Nicolini M (2004) Climatology of the low-level jet east of the Andes as derived from NCEP-NCAR reanalyses: characteristics and temporal variability. J Clim 17:2261–2280. https://doi.org/10.1175/1520-0442(2004)017%3c2261:cotlje%3e2.0.co;2

Marianetti G, Rivera JA, Bettolli ML (2024) Evaluation and selection of CMIP6 GCMs for the characterization of temperature and precipitation in Central-Western Argentina. Theor Appl Climatol 155:8185–8207. https://doi.org/10.1007/s00704-024-05123-1

Martinez JA, Dominguez F (2014) Sources of atmospheric moisture for the La Plata River Basin. J Clim 27:6737–6753. https://doi.org/10.1175/JCLI-D-14-00022.1

Martinez JA, Arias PA, Junquas C, Espinoza JC, Condom T, Dominguez F, Morales JS (2022) The Orinoco low-level jet and the cross-equatorial moisture transport over tropical South America: Lessons from seasonal WRF simulations. J Geophys Res Atmos 127:e2021JD035603. https://doi.org/10.1029/2021JD035603

Monteverde C, de Sales F, Jones C (2022) Evaluation of the CMIP6 Performance in Simulating Precipitation in the Amazon River Basin. Climate 10:122. https://doi.org/10.3390/cli10080122

Morales JS, Arias PA, Martínez JA, Durán-Quesada AM (2021) The role of low-level circulation on water vapor transport to Central and northern South America: insights from a 2D lagrangian approach. Int J Climatol 41:E2662–E2682. https://doi.org/10.1002/joc.6873

Müller GV, Repinaldo CRR, Araneo DC (2018) Extreme cold events in South America analyzed from a GFDL model perspective: comparison between CMIP3 and CMIP5 climate scenarios. Theor Appl Climatol 134:453–466. https://doi.org/10.1007/s00704-017-2286-3

Muñoz R, Garreaud R (2005) Dynamics of the low-level jet off the subtropical west coast of South America. Mon Weather Rev 133:3661–3677. https://doi.org/10.1175/mwr3074.1

Olmo ME, Balmaceda-Huarte R, Bettolli M (2022a) Multi-model ensemble of statistically downscaled GCMs over southeastern South America: historical evaluation and future projections of daily precipitation with focus on extremes. Clim Dyn 59:3051–3068. https://doi.org/10.1007/s00382-022-06236-x

Olmo ME, Espinoza JC, Bettolli ML, Sierra JP, Junquas C, Arias PA, Moron V, Balmaceda-Huarte R (2022b) Circulation patterns and associated rainfall over south tropical South America: GCMs evaluation during the dry-to-wet transition season. J Geophys Res Atmos 127:e2022JD036468. https://doi.org/10.1029/2022JD036468

Ortega G, Arias PA, Villegas JC, Marquet PA, Nobre P (2021) Present-day and future climate over central and South America according to CMIP5/CMIP6 models. Int J Climatol 41(15):6713–6735. https://doi.org/10.1002/joc.7221

Palomino-Lemus R, Córdoba-Machado S, Gámiz-Fortis SR, Castro-Díez Y, Esteban-Parra MJ (2015) Summer precipitation projections over northwestern South America from CMIP5 models. Glob Planet Change 131:11–23. https://doi.org/10.1016/j.gloplacha.2015.05.004

Palomino-Lemus R, Córdoba-Machado S, Gámiz-Fortis SR, Castro-Díez Y, Esteban-Parra MJ (2017) Climate change projections of boreal summer precipitation over tropical America by using statistical downscaling from CMIP5 models. Environ Res Lett 12:124011. https://doi.org/10.1088/1748-9326/aa9bf7

Peixoto JP, Oort AH (1992) Physics of climate. American Institute of Physics Melville, p 520

Pinto I, Jack C, Hewitson B (2018) Process-based model evaluation and projections over southern Africa from Coordinated Regional Climate Downscaling Experiment and Coupled

Model Intercomparison Project Phase 5 models. Int J Climatol 38:4251–4261. https://doi.org/10.1002/joc.5666
Poveda G, Mesa OJ (1999) The CHOCO low-level jet and two others jets over Colombia: climatology and variability during ENSO [in Spanish]. Revista De La Academia Colombiana De Ciencias Exactas, Físicas y Naturales 23:517–528
Poveda G, Mesa OJ, Salazar LF, Arias PA, Moreno HA, Vieira SC et al (2005) Diurnal cycle of precipitation in the tropical Andes of Colombia. Mon Weather Rev 133:228–240. https://doi.org/10.1175/mwr-2853.1
Poveda G, Waylen PR, Pulwarty R (2006) Modern climate variability in northern South America and southern Mesoamerica. Palaeogeogr Palaeoclimatol Palaeoecol 234:3–27. https://doi.org/10.1016/j.palaeo.2005.10.031
Poveda G, Jaramillo L, Vallejo LF (2014) Seasonal precipitation patterns along pathways of South American low-level jets and aerial rivers. Water Resour Res 50:98–118. https://doi.org/10.1002/2013WR014087
Poveda G, Espinoza JC, Zuluaga MD, Solman SA, Garreaud R, van Oevelen PJ (2020) High impact weather events in the Andes. Front Earth Sci 8:162. https://doi.org/10.3389/feart.2020.00162
Prado LF, Wainer I, Chiessi CM (2013) Mid-Holocene PMIP3/CMIP5 model results: intercomparison for the South American Monsoon System. The Holocene 23(12):1915–1920. https://doi.org/10.1177/0959683613505336
Rangel TF, Edwards NR, Holden PB, Diniz-Filho JAF, Gosling WD, Coelho MTP, Cassemiro FAS, Rahbek C, Colwell RK (2018) Modeling the ecology and evolution of biodiversity: Biogeographical cradles, museums, and graves. Science 361(6399):eaar5452. https://doi.org/10.1126/science.aar5452
Rao VB, Franchito SH, Rosa MB et al (2022) In a changing climate Hadley cell induces a record flood in amazon and another recorded drought across South Brazil in 2021. Nat Hazards 114:1549–1561. https://doi.org/10.1007/s11069-022-05437-1
Rau P, Bourrel L, Labat D, Melo P, Dewitte B, Frappart F et al (2016) Regionalization of rainfall over the Peruvian Pacific slope and coast. Int J Climatol 37(1):143–158. https://doi.org/10.1002/joc.4693
Reason CJC (2016) The Bolivian, Botswana, and Bilybara Highs and Southern Hemisphere drought/floods. Geophys Res Lett 43:1280–1286. https://doi.org/10.1002/2015GL067228
Reboita MS, Kuki CAC, Marrafon VH et al (2022) South America climate change revealed through climate indices projected by GCMs and Eta-RCM ensembles. Clim Dyn 58:459–485. https://doi.org/10.1007/s00382-021-05918-2
Rivera JA, Arnould G (2020) Evaluation of the ability of CMIP6 models to simulate precipitation over Southwestern South America: Climatic features and long-term trends (1901–2014). Atmos Res 241:104953. https://doi.org/10.1016/j.atmosres.2020.104953
Rojas M, Arias PA, Flores-Aqueveque V, Seth A, Vuille M (2016) The South American monsoon variability over the last millennium in climate models. Clim past 12:1681–1691. https://doi.org/10.5194/cp-12-1681-2016
Sakamoto M, Ambrizzi T, Poveda G (2011) Moisture sources and life cycle of convective systems over western Colombia. Adv Meteorol 2011:890759. https://doi.org/10.1155/2011/890759
Salio P, Nicolini M, Zipser EJ (2007) Mesoscale convective systems over southeastern South America and their relationship with the South American low-level jet. Mon Weather Rev 135:1290–1309. https://doi.org/10.1175/mwr3305.1
Segura H, Espinoza JC, Junquas C, Takahashi K (2016) Evidencing decadal and interdecadal hydroclimatic variability over the central Andes. Environ Res Lett 11:094016. https://doi.org/10.1088/1748-9326/11/9/094016
Segura H, Junquas C, Espinoza JC, Vuille M, Jauregui YR, Rabatel A, Condom T, Lebel T (2019) New insights into the rainfall variability in the tropical Andes on seasonal and interannual time scales. Clim Dyn 53:405–426. https://doi.org/10.1007/s00382-018-4590-8
Segura H, Espinoza JC, Junquas C, Vuille M, Garreaud R (2020) Recent changes in the precipitation-driving processes over the southern tropical Andes/western Amazon. Clim Dyn 54:2613–2631. https://doi.org/10.1007/s00382-020-05132-6
Seth A, Rauscher SA, Biasutti M, Giannini A, Camargo SJ, Rojas M (2013) CMIP5 projected changes in the annual cycle of precipitation in Monsoon regions. J Clim 26(19):7328–7351
Sierra JP, Arias PA, Vieira SC (2015) Precipitation over northern South America and its seasonal variability as simu-lated by the CMIP5 models. Adv Meteorol 2015:1–20. https://doi.org/10.1155/2015/634720
Sierra JP, Arias PA, Vieira SC, Agudelo J (2018) How well do CMIP5 models simulate the low-level jet in western Colombia? Clim Dyn 51(5–6):2247–2265. https://doi.org/10.1007/s00382-017-4010-5
Sierra JP, Arias PA, Durán-Quesada AM, Tapias KA, Vieira SC, Martínez JA (2021) The Choco low-level jet: past, present and future. Clim Dyn 56:2667–2692. https://doi.org/10.1007/s00382-020-05611-w
Silvestri G, Vera C (2009) Nonstationary impacts of the Southern Annular Mode on southern hemisphere climate. J Clim 22(22):6142–6148. https://doi.org/10.1175/2009jcli3036.1
Stuecker MF (2018) Revisiting the Pacific Meridional mode. Sci Rep 8:3216. https://doi.org/10.1038/s41598-018-21537-0
Sulca J, Vuille M, Silva Y, Takahashi K (2016) Teleconnections between the Peruvian Central Andes and Northeast Brazil during extreme rainfall events in austral summer. J Hydrometeorol 17:499–515. https://doi.org/10.1175/JHM-D-15-0034.1
Takahashi K (2012) Thermotidal and land-heating forcing of the diurnal cycle of oceanic surface winds in the eastern tropical Pacific. Geophys Res Lett 39:L04805. https://doi.org/10.1029/2011GL050692
Taschetto AS, Wainer I (2008) The impact of the subtropical South Atlantic SST on South American precipitation. Ann Geophys 26:3457–3476. https://doi.org/10.5194/angeo-26-3457-2008
Taylor KE (2001) Summarizing multiple aspects of model performance in a single diagram. J Geophys Res 106(D7):7183–7192. https://doi.org/10.1029/2000JD900719
Tedeschi RG, Collins M (2015) The influence of ENSO on South American precipitation during austral summer and autumn in observations and models. Int J Climatol 36:618–635. https://doi.org/10.1002/joc.4371
Torrealba ER, Amador JA (2010) La corriente en chorro de bajo nivel sobre los Llanos Venezolanos de Sur America. Rev Climatol 10:1–20
Vale MM, Arias PA, Ortega G, Cardoso M, Oliveira BFA, Loyola RD, Scarano FR (2021) Climate change and biodiversity in the Atlantic Forest: best climatic models, predicted changes and impacts, and adaptation options. In: Marques MCM, Grelle CEV (eds) The Atlantic forest. Springer, Cham, pp 253–267. https://doi.org/10.1007/978-3-030-55322-7_12
Valencia J, Mejía JF (2022) Projected changes of day-to-day precipitation and choco low-level jet relationships over the Far Eastern Tropical Pacific and Western Colombia from Two CMIP6 GCM Models. Atmos 13(11):1776. https://doi.org/10.3390/atmos13111776
Varuolo-Clarke AM, Smerdon JE, Williams AP, Seager R (2021) Gross discrepancies between observed and simulated twentieth-to-twenty-first-century precipitation trends in Southeastern South

America. J Clim 34(15):6441–6457. https://doi.org/10.1175/JCLI-D-20-0746.1

Vasconcellos FC, Deng Y, Zhang H, Martins G (2020) Austral summer precipitation biases over tropical South America in five CMIP5 earth system models. Int J Climatol 40:6506–6525. https://doi.org/10.1002/joc.6595

Vera C, Baez J, Douglas M, Emmanuel CB, Marengo J et al (2006a) The South American low-level jet experiment. Bull Am Meteorol Soc 87(1):63–78. https://doi.org/10.1175/BAMS-87-1-63

Vera C, Higgins W, Amador J, Ambrizzi T, Garreaud R, Gochis D, Gutzler D et al (2006b) Toward a unified view of the American Monsoon Systems. J Clim 19(20):4977–5000. https://doi.org/10.1175/JCLI3896.1

Viale M, Garreaud R (2015) Orographic effects of the subtropical and extratropical Andes on upwind precipitating clouds. J Geophys Res Atmos 120:4962–4974. https://doi.org/10.1002/2014jd023014

Viale M, Bianchi E, Cara L, Ruiz LE, Villalba R, Pitte P (2019) Contrasting Climates at Both Sides of the Andes in Argentina and Chile. Front Environ Sci 7:69. https://doi.org/10.3389/fenvs.2019.00069

Vicente-Serrano SM, García-Herrera R, Peña-Angulo D et al (2022) Do CMIP models capture long-term observed annual precipitation trends? Clim Dyn 58:2825–2842. https://doi.org/10.1007/s00382-021-06034-x

Vuille M, Bradley RS, Keimig F (2000) Climate variability in the Andes of Ecuador and its relation to tropical Pacific and Atlantic sea surface temperatures anomalies. J Clim 13:2520–2535. https://doi.org/10.1175/1520-0442(2000)013%3c2520:CVITAO%3e2.0.CO;2

Wang C (2007) Variability of the Caribbean Low-Level Jet and its relations to climate. Clim Dyn 29:411–422. https://doi.org/10.1007/s00382-007-0243-z

Yepes J, Poveda G, Mejía JF, Moreno L, Rueda C (2019) CHOCO-JEX. a research experiment focused on the Chocó Low-Level Jet over the Far Eastern Pacific and Western Colombia. Bull Am Meteorol Soc 100:779–796. https://doi.org/10.1175/bams-d-18-0045.1

Yin L, Fu R, Shevliakova E, Dickinson RE (2013) How well can CMIP5 simulate precipitation and its controlling processes over tropical South America? Clim Dyn 41:3127–3143. https://doi.org/10.1007/s00382-012-1582-y

Yoon JH, Zeng N (2010) An Atlantic influence on Amazon rainfall. Clim Dyn 34:249–264. https://doi.org/10.1007/s00382-009-0551-6

Zazulie N, Rusticucci M, Raga GB (2018) Regional climate of the Subtropical Central Andes using high-resolution CMIP5 models. Part II: future projections for the twenty-first century. Clim Dyn 51:2913–2925. https://doi.org/10.1007/s00382-017-4056-4

Zhang G, Wang Z (2013) Interannual variability of the Atlantic Hadley circulation in boreal summer and its impacts on Tropical Cyclone Activity. J Clim 26(21):8529–8544. https://doi.org/10.1175/JCLI-D-12-00802.1

Zhang MZ, Xu Z, Han Y et al (2024) Evaluation of CMIP6 models toward dynamical downscaling over 14 CORDEX domains. Clim Dyn 62:4475–4489. https://doi.org/10.1007/s00382-022-06355-5

Zhou J, Lau K-M (1998) Does a monsoon climate exist over South America? J Clim 11(5):1020–1040. https://doi.org/10.1175/1520-0442(1998)011%3c1020:DAMCEO%3e2.0.CO;2